A Weak Penalty Neural ODE for Learning Chaotic Dynamics from Noisy Time Series

Xuyang Li[©], ^{1, 2, *} John Harlim, ¹ Dibyajyoti Chakraborty[©], ¹ and Romit Maulik[©], [†]

¹ The Pennsylvania State University, University Park, PA 16802, USA

² University of North Carolina at Charlotte, Charlotte, NC 28223, USA

(Dated: November 24, 2025)

Accurate forecasting of complex high-dimensional dynamical systems from observational data is essential for several applications across science and engineering. A key challenge, however, is that real-world measurements are often corrupted by noise, which severely degrades the performance of data-driven models. Particularly, in chaotic dynamical systems, where small errors amplify rapidly, it is challenging to identify a data-driven model from noisy data that achieves short-term accuracy while preserving long-term invariant properties. In this paper, we propose the use of the weak formulation as a complementary approach to the classical strong formulation of data-driven time-series forecasting models. Specifically, we focus on the neural ordinary differential equation (NODE) architecture. Unlike the standard strong formulation, which relies on the discretization of the NODE followed by optimization, the weak formulation constrains the model using a set of integrated residuals over temporal subdomains. While such a formulation yields an effective NODE model, we discover that the performance of a NODE can be further enhanced by employing this weak formulation as a penalty alongside the classical strong formulation-based learning. Through numerical demonstrations, we illustrate that our proposed training strategy, which we coined as the Weak-Penalty NODE (WP-NODE), achieves state-of-the-art forecasting accuracy and exceptional robustness across benchmark chaotic dynamical systems and real-world climate dataset.

The accurate prediction of complex dynamical systems is of vital importance to science and engineering [1, 2], with applications ranging from weather forecasting and climate modeling to fluid dynamics and systems biology. Traditional high-fidelity simulations are computationally expensive and often diverge from real-world data [3, 4]. Whereas data-driven methods [5–9], particularly those based on machine learning [10–12], have emerged as a powerful tool for learning these system dynamics directly from observational data and offer a computationally efficient alternative to first-principles simulation.

A variety of machine learning models have shown strong performance in forecasting complex spatiotemporal dynamics, including recurrent models [13, 14] such as Long Short-Term Memory (LSTM) [14–16], reservoir computing (RCs) [14, 17–19], temporal convolutional networks (TCNs) [20, 21], attention-based Transformers [22–24], and more recently, random feature maps (RFMs) [25]. However, these models treat dynamics as a discrete-time autoregressive process, predicting each step from the last. This leads to error accumulation over long horizons and fails to capture invariant properties, such as probability density functions (PDFs), spectral characteristics, and attractors, limiting robustness to extended long-term forecasting. These issues are further exacerbated in the presence of observation noise.

Rather than learning discrete transitions, Neural Ordinary Differential Equations (Neural ODEs or NODEs) [26, 27] model dynamics by parameterizing the derivative of the state with a neural network. By leveraging modern ODE solvers, NODEs enable inference at arbitrary time points. This continuous formulation enables a flexible accuracy-speed trade-off and achieves substantially lower error than RNNs on time-series predic-

tion [26]. Furthermore, NODEs offer architectural flexibility, with dynamics modeled by anything from simple feedforward networks to convolution [28], U-Net [28, 29], or transformer, enabling the capture of complex spatial and temporal dependencies beyond traditional recurrent models.

However, training NODEs remains challenging in practice. Standard NODE training uses the adjoint sensitivity method [26, 30, 31], which, despite its memory efficiency, incurs high computational cost from repeated ODE forward and backward solves. Moreover, backward integration is often unstable, with exploding or vanishing gradients [32–35], especially in stiff systems [36, 37]. Additionally, vanilla NODEs do not inherently guarantee stable long-horizon rollouts; achieving robustness typically requires additional architectural constraints or specialized training techniques [32, 33].

Most importantly, observational noise in real-world data severely limits the utility of this continuous-time framework [38, 39]. Pointwise losses force the model to fit noisy trajectories, making the learned dynamics overly sensitive to high-frequency fluctuations. This often degrades prediction accuracy and causes instability during inference, especially in chaotic systems where small errors can rapidly amplify into forecast failure [25, 40].

In response to the challenge of learning from noisy data, Bayesian and probabilistic models such as Gaussian Process-based approaches [41–43] and Bayesian neural surrogates [44, 45] offer principled uncertainty quantification, but often struggle with high computation cost, sensitivity to hyperparameters, restrictive modeling assumptions, and costly inference. Neural SDEs [46] extend probabilistic models by learning drift and diffusion terms, but focus on uncertainty modeling rather than re-

covering deterministic dynamics. The extended Kalman filter [47] estimates states recursively under noise but relies on known dynamics and linearization, which often fail in nonlinear settings. Notably, Galerkin-based methods employ weak formulations by projecting residuals onto test functions and minimizing integral errors, which naturally suppresses high-frequency noise. This weak-form spirit has inspired broader models [48–50], including weak-form or variational physics-informed neural networks (PINNs) [51, 52], weak-SINDy [40, 53], improving robustness by integrating residuals over subdomains. One recent work on weak-form NODEs [54] focuses on accelerating training and shows a promising speed-up, though its predictive accuracy does not consistently outperform baseline NODEs.

This reflects a key trade-off: integral nature provides robustness against noise but may potentially compromise predictive fidelity. Crucially, weak-form methods constrain dynamics only indirectly, bypassing the explicit forward simulation that serves as the ultimate test of a predictive model. In contrast, strong-form methods, though highly sensitive to noise, directly optimize pointwise residuals for high local fidelity. These complementary strengths and their respective shortcomings motivate a combined weak-strong training framework that reconciles the statistical stability of weak-form training with the local fidelity of strong-form supervision, especially under noisy conditions.

To mitigate this issue, we propose WP-NODE, a synergistic-form learning approach that combines weak and strong supervision within a NODE framework to robustly learn the dynamics of complex systems from noisy observational data. This method integrates the statistical robustness of weak-form training with the local accuracy of strong-form supervision, enabling the model to recover both the long-term statistical structure and the short-term dynamics of the system. Specifically, the training is guided by a unified loss function that combines shorter pointwise trajectory errors with weak-form residuals integrated against a set of test functions.

In the following sections, WP-NODE demonstrates its versatility and efficacy across four chaotic systems, including the 3-dimensional Lorenz-63 system, the 40-dimensional Lorenz-96 system, the 64-dimensional Kuramoto–Sivashinsky system, and a real-world climate dataset, ERA5. Our results show that this weak penalty formulation consistently improves both short-term predictive accuracy and long-term statistical consistency, offering a new perspective on robust data-driven modeling of complex dynamical systems.

RESULTS

Summary of Key Findings. The key results in this section can be summarized as follows. While weak-

form supervision achieves relatively high short-term accuracy in local regions, its statistical consistency deteriorates, as revealed by significant invariant measure mismatches. In contrast, strong-form supervision captures the correct statistical distribution but suffers from poor short-term prediction accuracy due to training on noisy data. The proposed WP-NODE, however, balances both aspects, achieving accurate short-term prediction and faithful long-term statistical behavior.

Evaluation Metrics. To assess both short-term accuracy and long-term consistency, we use two complementary metrics: Valid Prediction Time (VPT) and Kullback–Leibler (KL) divergence [55]. The VPT is defined as the maximum duration (in units of Lyapunov time, $T_{\Lambda} = 1/\Lambda$, where Λ is the system's maximal Lyapunov exponent), for which the normalized trajectory error remains below a certain error tolerance ε ,

$$VPT = \frac{1}{T_{\Lambda}} \max \{ n\Delta t \mid E_k \le \varepsilon \text{ for all } k \le n \}.$$
 (1)

Here, the normalized error (at time step n) is defined as $E_n = \sqrt{\frac{\sum_{j=1}^D (\hat{u}_j(n\Delta t) - u_j(n\Delta t))^2}{\sum_{j=1}^D \sigma_j^2}}$. D is the dimension of the system and σ_j is the standard deviation of the j-th component of the true trajectory.

For long-term statistical consistency, the probability density function (PDF) of the surrogate model is estimated and compared to that of the reference system using the KL divergence. This comparison is performed dimension-wise via histogram-based approximations of the invariant measures. Visual comparisons of distributional statistics are also used to validate long-term behavior when KL divergence fails to reflect perceptual differences.

Lorenz-63. To illustrate the contrast between trajectory accuracy and statistical faithfulness, the 3D L63 [56] system is first considered. The governing equation is:

$$\frac{dx}{dt} = \sigma(y - x),$$

$$\frac{dy}{dt} = x(\rho - z) - y,$$

$$\frac{dz}{dt} = xy - \beta z$$
(2)

The well-known butterfly-like attractor can be reproduced under the standard parameters $\sigma=10.0$, $\rho=28.0$, and $\beta=\frac{8}{3}$. In our numerical experiment, we integrate this system of ODEs using the RK4 scheme with a time step of $\Delta t=0.01s$ for 100s, yielding $N=10^4$ samples. Evaluation is based on a validation threshold of $\varepsilon=0.3$. Under these parameters, the largest Lyapunov exponent is $\Lambda\approx0.91$.

First, 5% data noise is applied to the observation data, where a zero-mean Gaussian is defined with standard deviation $\sigma = \sigma_{\rm NR} \cdot {\rm RMS}(x)$, based on the root-mean-

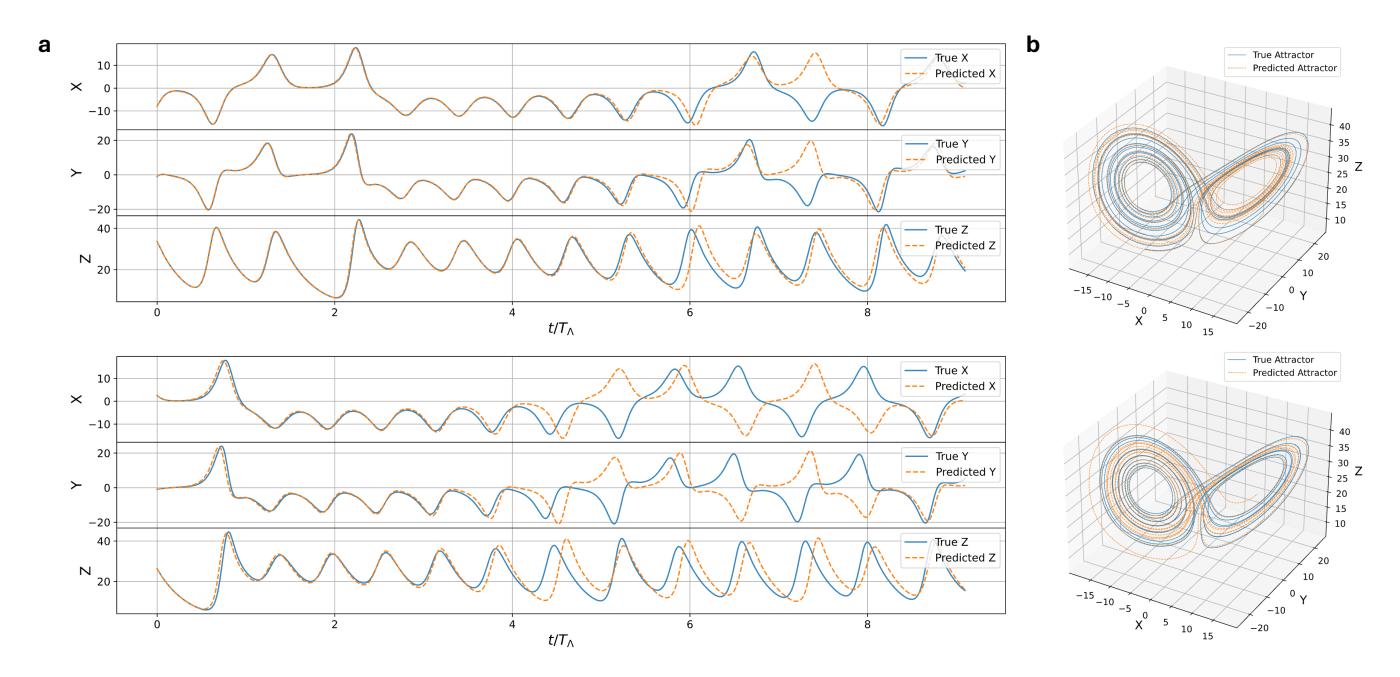


FIG. 1. Forecasting of the Lorenz-63 system using WP-NODE under 5% training data noise. **a.** Time-series comparison between predicted and ground-truth trajectories for all three state variables. Rows show the best (VPT = 5.77) and worst (VPT = 0.63) cases (x-axis in Lyapunov time). Despite low VPT in the second case, predictions remain accurate for about 4 Lyapunov times. **b.** Reconstructed phase-space attractors for the predicted (orange) and true attractor (blue).

square of the clean signal. The behavior of the trained WP-NODE model is illustrated in Fig. 1, demonstrating its great capabilities in both short-time prediction and attractor recovery. Specifically, Fig. 1a shows two representative trajectories corresponding to the best and worst predictions, selected from different initial conditions. The resulting VPT varies between 0.63 and 5.77 Lyapunov times. Despite the lower VPT in the second case, the prediction remains visually accurate for nearly 4 Lyapunov times before diverging. Figure 1b shows the corresponding Lorenz attractors, indicating that the WP-NODE robustly recovers the long-term statistical behavior of the system.

To complement the trajectory-based evaluation, Fig. 2 compares the predicted and ground-truth invariant measures using PDFs of the X component, for simplicity. These PDFs represent the system's invariant measure across all methods and noise levels. Four methods, the proposed WP-NODE, and three baselines (strong NODE, weak NODE, and DeepSkip [25]) are compared. All methods perform well under very low noise (1%). However, as noise increases to 5%, DeepSkip performance deteriorates, indicating high sensitivity to data perturbations. At higher noise levels (10% and 20%), both the strong and weak NODE also fail to recover the correct invariant measure, demonstrating a clear breakdown in statistical consistency under heavy noise. In contrast, WP-NODE remains robust, preserving a reasonable approximation of the true distribution even under 20% noise.

Table I reports the VPT and KL divergence metric un-

der varying noise levels (0%, 1%, 5%, 10%, and 20%), for all four methods. As shown on the left side of the table, for the L63 system, WP-NODE consistently outperforms both strong and weak NODE baselines under noisy conditions. This improvement can be attributed to two effects. When noise is low, the strong-form component provides stability and accuracy, enhancing short-term prediction. As noise increases, strong-form supervision becomes unreliable due to error amplification in pointwise residuals. In those regimes, the weak-form loss plays a dominant role in preserving local coherence. Notably, even at 20% noise, WP-NODE maintains high predictive accuracy, outperforming the weak form with a 14% gain in VPT. In contrast, DeepSkip, a leading baseline under clean data, deteriorates sharply with even small noise, highlighting the robustness of our proposed formulation.

Similarly, the right side of Table I reports the mean KL divergence metric as we defined above. While the KL metric tends to be small under low noise, due to the low-dimensional structure of the Lorenz attractor, WP-NODE continues to preserve lower values of KL, suggesting long-term statistical consistency, even at 10% and 20% noise levels. However, KL divergence becomes less informative at high values, as it may overlook localized distributional mismatches. To complement this, Supplementary Note 1 provides visual comparisons of the invariant measure (PDFs) for all three components across noise levels. These plots show that WP-NODE consistently preserves the true distribution, while baselines degrade significantly under high noise, highlighting the su-

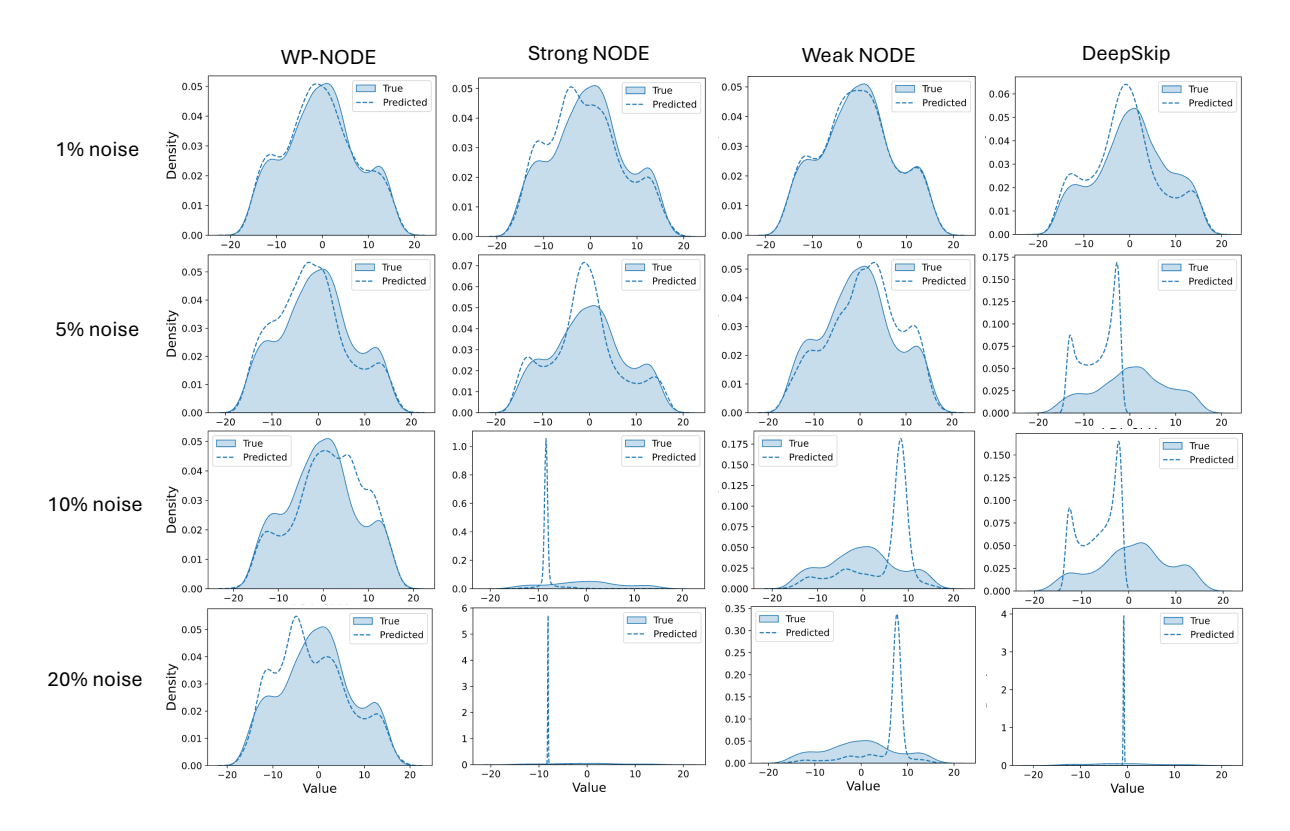


FIG. 2. Invariant measure of the predicted Lorenz-63 system (for 100s) for the X components beyond the training region, across different data noise. The proposed method maintains strong agreement with the ground truth across all noise levels, preserving long-term statistical properties. Other methods deteriorate significantly under moderate to high noise.

		VPT (Lyapunov times) ↑					KL divergence ↓				
System	Method	0%	1%	5%	10%	20%	0%	1%	5%	10%	20%
L63	WP-NODE	3.01 ± 1.38	3.11 ± 1.81	2.70 ± 1.13	1.63 ± 0.68	1.12 ± 0.76	0.06	0.02	0.03	0.04	0.04
	Strong NODE	2.65 ± 0.99	2.58 ± 1.07	1.40 ± 0.64	0.83 ± 0.42	0.34 ± 0.14	0.03	0.04	0.09	3.98	16.29
	Weak NODE	2.67 ± 1.29	2.85 ± 1.40	2.29 ± 1.12	1.60 ± 0.84	0.98 ± 0.54	0.03	0.02	0.03	0.65	1.25
	DeepSkip	$\textbf{4.06} \pm 1.15$	1.29 ± 0.59	0.46 ± 0.26	0.24 ± 0.15	0.09 ± 0.08	0.02	0.05	10.80	12.19	18.82
L96	WP-NODE	3.65 ± 0.64	3.72 ± 0.63	$\textbf{3.24} \pm 0.64$	2.75 ± 0.61	$\textbf{2.10} \pm 0.52$	0.09	0.09	0.10	0.12	0.09
	Strong NODE	2.80 ± 0.68	2.74 ± 0.58	2.57 ± 0.42	1.94 ± 0.38	1.23 ± 0.26	0.08	0.08	0.11	0.19	1.38
	Weak NODE	3.66 ± 0.65	3.80 ± 0.66	3.19 ± 0.69	2.71 ± 0.62	2.10 ± 0.52	0.09	0.08	0.09	0.10	0.10
	DeepSkip	$\textbf{6.02} \pm 1.03$	$\textbf{4.32} \pm 0.71$	1.64 ± 0.34	0.92 ± 0.16	0.56 ± 0.13	0.09	0.09	0.27	0.64	1.39
KS	WP-NODE	3.38 ± 0.79	3.71 ± 1.17	3.31 ± 0.95	2.87 ± 0.97	1.53 ± 0.58	1.65	1.60	1.74	1.71	0.48
	Strong NODE	2.61 ± 0.74	2.49 ± 0.42	2.45 ± 0.76	1.88 ± 0.60	1.32 ± 0.40	2.17	2.17	1.54	2.14	2.46
	Weak NODE	$\textbf{3.49} \pm 0.92$	$\textbf{3.82} \pm 0.66$	1.97 ± 0.46	2.42 ± 0.89	0.44 ± 0.11	1.61	1.49	2.20	2.33	11.10

TABLE I. Cross-system evaluation (L63, L96, KS) under different observation noises. VPT is reported as mean \pm std in Lyapunov times; KL divergence is reported as the mean value. The VPT evaluation is performed 30 times at random starting points beyond the training region. Higher is better for VPT, lower is better for KL divergence.

perior robustness and statistical fidelity of the proposed method.

To further evaluate robustness and generalizability, a comprehensive sensitivity analysis was conducted on the L63 system by varying key hyperparameters and training configurations. As shown in *Supplementary Note 2*, such

a weak penalty formulation remains stable across a wide range of settings, highlighting its resilience to architectural and optimization choices.

In addition, Supplementary Note 2 also provides a comparison of the training speed, where WP-NODE is evaluated with varying numbers of rollouts on the L63

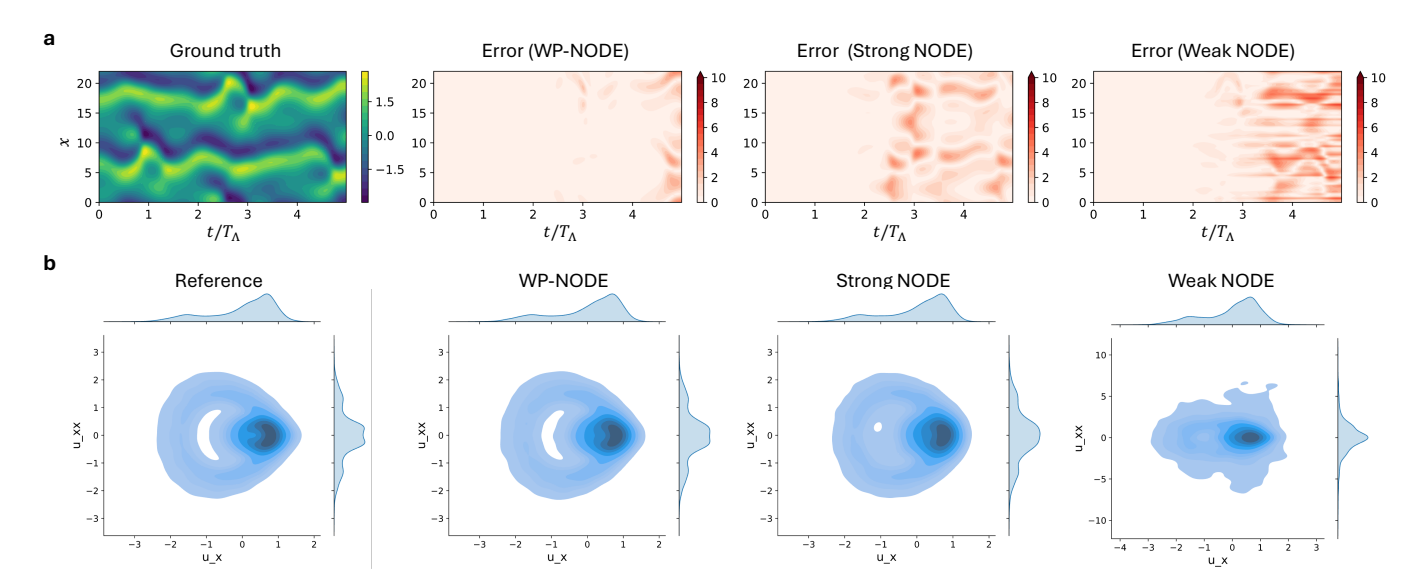


FIG. 3. Performance comparison of WP-NODE and baselines models on the KS system, under 5% data noise. DeepSkip is not included since the original work was analyzed on a different configuration and would require task-specific fine-tuning. a. Short-time prediction comparison of the learned KS system under 5% observation noise. b. Joint probability density for the KS system under 5% observation noise. Both the WP-NODE and strong NODE closely reproduce the reference distribution, with WP-NODE showing slightly improved alignment in the core region. The weak NODE, however, exhibits notable distortion in the invariant measure.

system. Results show a substantial speedup of $8.6\times$ over strong NODE (slowed by adjoint computations), with only minor degradation relative to weak NODE. This demonstrates a favorable trade-off between efficiency and performance.

Lorenz-96. To evaluate performance on high-dimensional chaotic dynamics, WP-NODE is tested on the 40D L96 model [57],

$$\frac{dx_i}{dt} = (x_{i+1} - x_{i-2})x_{i-1} - x_i + F, \quad i = 1, \dots, d, \quad (3)$$

with cyclic boundary conditions $x_{i\pm kd} = x_i$ and forcing F = 10. The system is integrated with step size $\Delta t = 0.01$ for 1000 seconds ($N = 10^5$ steps). We measure the VPT with $\varepsilon = 0.5$. This setup yields a leading Lyapunov exponent of $\Lambda \approx 1.68$ [25].

As shown in Table I, all methods achieve comparable performance on this 40-dimensional L96 system, with only marginal differences in both VPT and KL divergence across noise levels. This similarity in performance may stem from the high-dimensional mixing of the system, which limits the discriminative power of standard metrics, or from inherent limitations of NODE-based methods in capturing fine-grained chaotic dynamics. Nonetheless, WP-NODE remains robust across all noise intensities, maintaining consistent predictive and statistical performance in this high-dimensional chaotic system. Additional comparisons and visualizations are provided in Supplementary Note 3.

Kuramoto-Sivashinsky. The KS equation [58, 59] is

a canonical benchmark for spatiotemporal chaos in nonlinear PDEs. It describes the evolution of a field u(x,t)governed by

$$\frac{\partial u}{\partial t} + u \frac{\partial u}{\partial x} + \frac{\partial^2 u}{\partial x^2} + \frac{\partial^4 u}{\partial x^4} = 0, \tag{4}$$

where chaotic behavior emerges from the interaction between nonlinearity, instability, and dissipation.

The system is discretized using 64 Fourier modes on a periodic domain of length 22, and integrated for $N=10^5$ steps with a time step of $\Delta t=0.25$, yielding a 25,000s trajectory. We measure the VPT with $\varepsilon=0.5$. In this regime, the largest Lyapunov exponent is approximately $\Lambda\approx0.05$ [59].

Fig. 3a presents the short-time prediction skill of WP-NODE and related baselines on the KS system, where these models are trained with timeseries corrupted by 5% noise. We note that WP-NODE faithfully reproduces the dominant spatiotemporal structures, achieving a mean VPT of 3.31 (see Table I). In contrast, strong and weak NODEs exhibit increasing phase drift and amplitude decay, with shorter predictive windows of 2.45 and 1.97, respectively. DeepSkip is excluded due to tuning difficulties and because the original work was trained on a different configuration [25].

Fig. 3b highlights WP-NODE's ability to recover accurate long-term statistics via joint probability density plots. Under 5% observation noise, both WP-NODE and the strong NODE approximate the reference invariant distribution, but only WP-NODE captures both the core

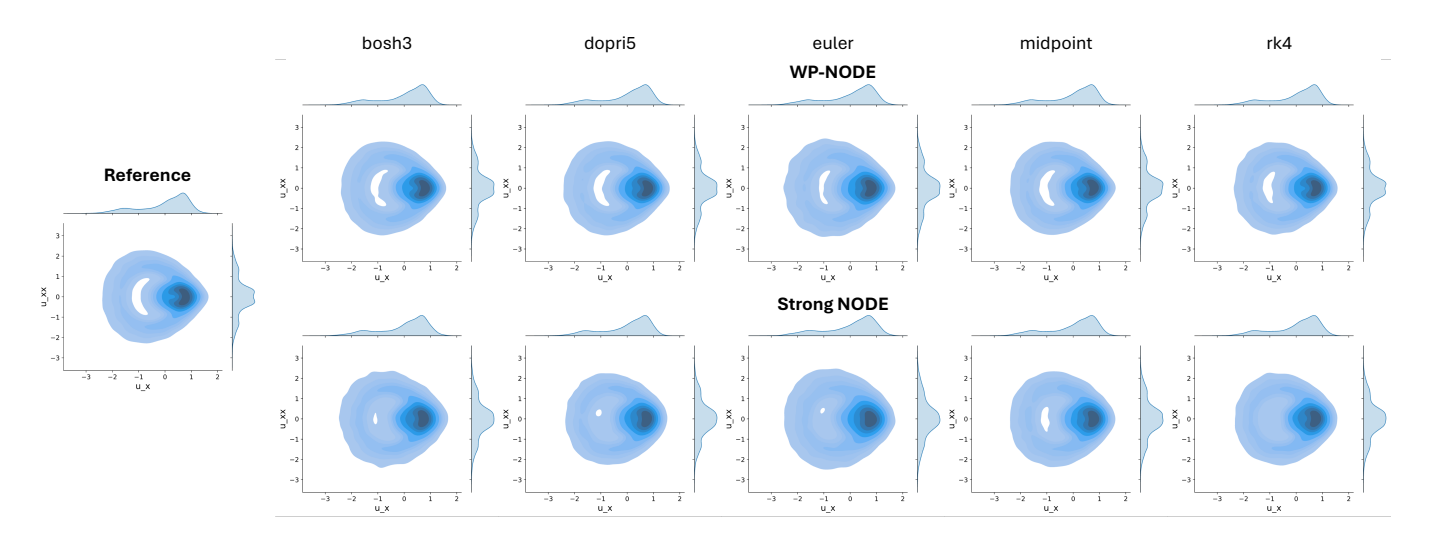


FIG. 4. Comparison of the long-term behavior of the KS system under 5% data noise, using the invariant measure (i.e., joint probability density). In the first row, WP-NODE shows more consistent results than the strong NODE in the second row, demonstrating its solver-agnostic property.

and tail behaviors with high fidelity. In contrast, the weak-form baseline fails to reproduce the full statistical structure, indicating degraded long-horizon dynamics.

Table I further reports robustness under different signal-to-noise ratios. WP-NODE maintains stable performance under perturbations, achieving a VPT of 2.87 at 10% noise, while the strong NODE baseline drops to 1.88. At higher noise levels, WP-NODE's variant continues to outperform both baselines, highlighting its superior robustness. Interestingly, the weak NODE baseline shows erratic behavior: its VPT at 5% noise (1.97) is even lower than at 10% (2.42), indicating instability in dynamics reconstruction, consistent with prior findings [54]. In contrast, WP-NODE remains stable across noise levels. Overall, these results underscore a key strength of WP-NODE: it extends predictive horizons under noise while preserving the statistical properties of chaotic spatiotemporal systems, crucial for reliable long-term modeling.

Note that with 20% noise, WP-NODE utilizes 5 rollouts, which is found to be more effective for short-time prediction compared to lower-noise cases, where only a single rollout is used. This longer rollout strategy significantly improves VPT on the KS system, potentially because exposure to longer temporal contexts during training helps the model better distinguish signal from noise. In Supplementary Note 7, we provide the details of how many rollouts are used for each case in Table I.

To further examine solver dependence, the trained model (using the dopri5 solver) was integrated under different numerical integration schemes, including bosh3, euler, midpoint, and rk4, for a 600s prediction (approximately 30 Lyapunov times) with 5% observation noise. As shown in Fig. 4, the strong NODE, despite being trained with 25-step rollouts, produces varying invariant measures across solvers, highlighting its sensi-

tivity to the discretization scheme used during training. The weak NODE, lacking any rollout-based supervision, fails to capture long-term dynamics and becomes unstable across all solvers. Thus, we omit showing the joint probability density estimates from various ODE solvers. In contrast, the WP-NODE model produces density estimates that are not only qualitatively similar to the reference densities but also robust under different choices of ODE solvers. This empirical result suggests that the model has learned the underlying continuous-time dynamics in a solver-agnostic manner. This addresses a key limitation of purely weak or strong NODEs, whose predictive capability is typically either sensitive to time discretization or unstable during long-term integration.

ERA5 atmospheric reanalysis dataset. To evaluate WP-NODE in a high-dimensional, noisy, and strongly coupled real-world setting, experiments are conducted on the ERA5 atmospheric reanalysis dataset with a temporal resolution of 6 hours from January 1, 2000 to December 15, 2009 [60]. The data are regridded to a T30 Gaussian grid and vertically interpolated onto σ -levels [61], yielding input tensors of four prognostic variables, including near-surface temperature (t) and specific humidity (q) at $\sigma_{0.95}$, and mid-atmospheric zonal (u) and meridional (v) winds at $\sigma_{0.51}$. The horizontal resolution of each variable consists of 48 latitude times 96 longitudinal data points. Total Incoming Solar Radiation (TISR) is added as a temporal embedding to capture external radiative forcing [32, 62].

A CNN-based NODE architecture is employed for this spatio-temporal dataset. Following model training, we assess and compare both short- and long-term predictive capacity of WP-NODE against the baseline weak and strong NODEs. In the short-term (Fig. 5a, 14 days), both weak and strong NODEs quickly become unstable

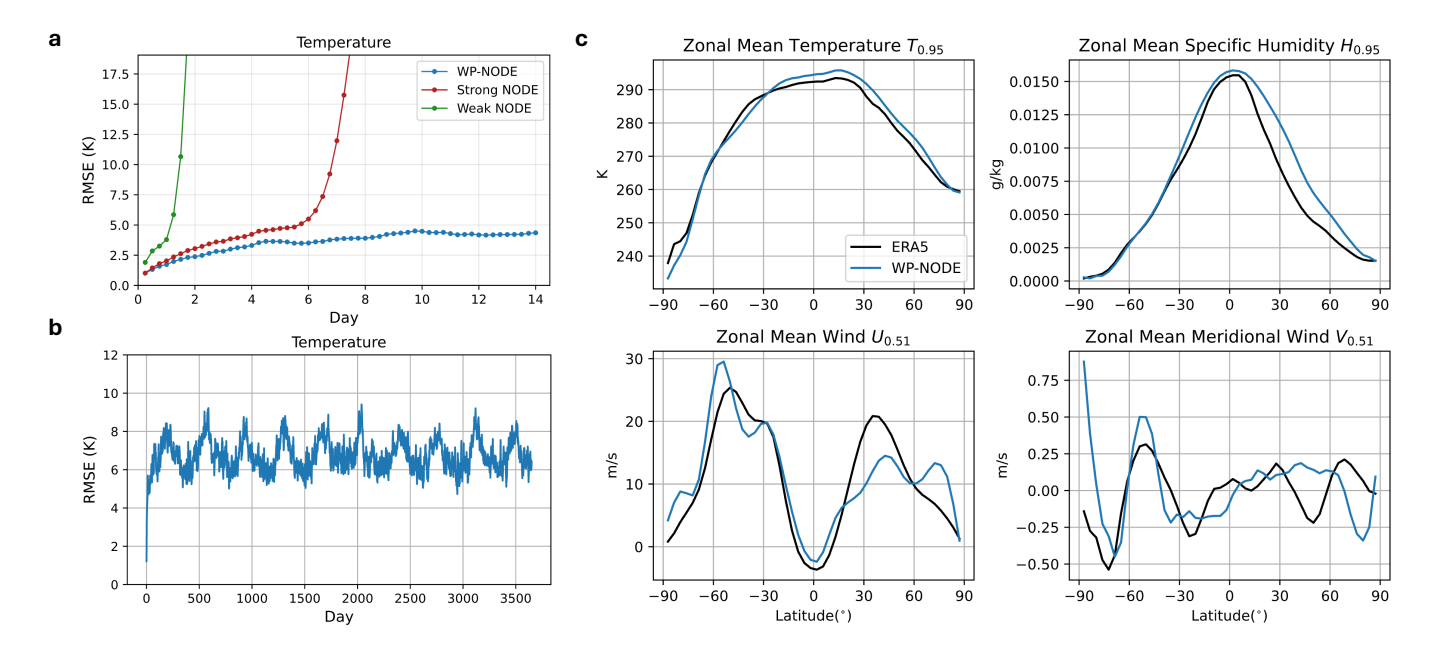


FIG. 5. NODE predictions performance on real-world ERA5 dataset. a. Short-term (14-day) temperature prediction errors. WP-NODE achieves the lowest error. b. Long-term (10-year) temperature prediction errors. WP-NODE remains stable. c. Climatological statistical prediction for 10 years of WP-NODE across the four ERA5 prognostic variables.

and show rapidly increasing errors, whereas WP-NODE consistently achieves the lowest RMSE. Even over a 10year horizon (Fig. 5b), WP-NODE remains stable, while both baseline NODEs diverge. Figure 5c further evaluates the predicted climatological statistics. For each variable, the temporal average over the 10-year testing period is computed. The zonal mean at each latitude is then obtained by averaging the time-averaged field along the longitude direction. Notice that WP-NODE produces accurate predictions of both the zonal mean temperature and specific humidity. While the prediction for the average zonal and meridional winds is less accurate, WP-NODE is able to capture their trend relatively well. Detailed configurations and additional performance comparisons, including extended 1-year predictions for other prognostic variables, are provided in Supplementary Note 4.

Overall, the ERA5 experiment highlights the robustness of our hybrid training strategy and demonstrates that, even with a simple CNN-based architecture, WP-NODE delivers superior stability, accuracy, and long-term predictive fidelity on real-world climate data, where both weak and strong NODEs deteriorate.

CONCLUSION AND DISCUSSION

This work introduces a weak penalty in training NODE, named WP-NODE, for learning chaotic dynamical systems from noisy data. Particularly, the proposed approach mitigates the lack of prediction skill of a standard NODE trained with a strong form formula-

tion when the training data are corrupted by noise. Furthermore, the strong form NODE model's long-term statistical prediction accuracy is sensitive to the choice of the ODE integrator. WP-NODE, by contrast, exhibits greater independence from the specific numerical solver employed, enhancing its robustness across different integration schemes.

While weak-form supervision alone achieves relatively high predictive horizons, it lacks statistical fidelity. We found that the proposed WP-NODE effectively reconciles both extended prediction time and robustly preserves long-term statistical structure. Across four chaotic systems, L63, L96, KS, and a climate forecasting benchmark, WP-NODE consistently delivers accurate short-term forecasts and preserves faithful long-term statistics, even under substantial observational noise. Furthermore, application to the ERA5 climate reanalysis dataset demonstrates that WP-NODE maintains stable and accurate long-term forecasts even with a simple CNN-based architecture, where strong and weak NODE approaches quickly diverge.

WP-NODE also offers substantial training efficiency, achieving over $8.6\times$ faster per-epoch training compared to full strong-form NODEs, while maintaining comparable speed to the baseline weak-form approach. This efficiency is enabled by the use of a single-step rollout and adjoint-free backpropagation, significantly reducing memory and computational overhead. Although a single-step rollout is sufficient in most scenarios, additional rollout steps (≤ 5) can further enhance predictive accuracy in certain systems, revealing a flexible trade-off between

performance and computational cost. This is a significant computational reduction since the results of the strong NODE model reported in Table I fit the data for at least 25 steps of rollouts.

Beyond efficiency, WP-NODE benefits from its combined weak–strong structure: the weak formulation naturally mitigates overfitting compared to pure pointwise losses, while the strong-form rollout enhances numerical stability by explicitly solving the underlying ODE. In many cases, the weak form alone trains successfully but fails at inference time due to exponentially exploding dynamics, making our approach particularly effective for learning from noisy data.

We note that the implemented weak formulation adopts predefined subdomain sizes and fixed test functions, which may influence performance in certain settings. While extensive ablation studies confirm robustness across a range of configurations, further improvements may be possible through adaptive subdomain partitioning, learnable test functions, or task-specific architectural tuning, particularly for more complex or higher-dimensional systems.

Overall, this study demonstrates that combining weak and strong supervision offers a simple yet effective route toward noise-robust, statistically consistent learning of chaotic dynamics, supporting both generalizability and extensibility to more complex systems.

METHOD

Neural Ordinary Differential Equations. NODEs [26] generalize residual networks by replacing discrete-layer architectures with a continuous-time dynamics model. Given an initial condition $u(t_0) = u_0$, the evolution of the state is governed by:

$$\frac{du(t)}{dt} = f(u(t), t; \theta), \tag{5}$$

where f is a neural network parameterized by θ . The solution at a later time t is determined by solving this initial value problem using standard adaptive ODE solvers (e.g., Runge–Kutta, Dormand–Prince) [63, 64], which adjust their step size to balance computational cost and precision.

Strong Formulation and Adjoints. The standard training paradigm for a NODE is the strong formulation, which enforces that the predicted trajectory $\hat{u}(t)$ closely matches the ground-truth state u(t). This objective is typically achieved by minimizing a loss function, such as the mean squared error (MSE),

$$\mathcal{L}_{\text{strong}}(\theta) = \frac{1}{T} \sum_{n=0}^{T-1} \| u(t_n) - \hat{u}(t_n; \theta) \|^2, \qquad (6)$$

where T denotes the number of rollouts in training (set to T=25).

To optimize the parameters θ with respect to this loss, gradients are computed using the adjoint sensitivity method [26]. This approach provides exact gradients with constant memory cost, since intermediate forward states u(t) do not need to be stored. However, the gradient computation becomes prohibitively expensive for chaotic or stiff dynamics, especially for large T. Exploding gradients and numerical instabilities demand small solver step sizes and tight tolerances, leading to high computational overhead [32, 33, 36]. These limitations motivate alternative strategies, such as weak-form or multi-step formulations, to improve stability and efficiency.

Weak Formulation. The weak form recasts the NODE into an integral form by weighting it with smooth and compactly supported test functions. This approach avoids pointwise enforcement of dynamics, improves robustness to noisy data, and eliminates the need for numerical differentiation in the training.

Let ϕ be a smooth test function defined on the time interval [a,b], and satisfying $\phi(a)=\phi(b)=0$. The weak formulation of Eq. (5) requires that the residual is orthogonal to all test functions in an integral sense,

$$\int_{a}^{b} \left(\dot{u}(t) - f(u(t), t; \theta) \right) \phi(t) dt = 0.$$
 (7)

For numerical and theoretical advantages, we apply integration by parts to the derivative term $\int_a^b\phi(t)\dot{u}(t)dt$

$$\int_a^b \phi(t)\dot{u}(t)dt = \left[\phi(t)u(t)\right]_a^b - \int_a^b \dot{\phi}(t)u(t)dt.$$

The boundary contribution $\left[\phi(t)u(t)\right]_a^b$ vanishes because the test function satisfies $\phi(a)=\phi(b)=0$, leaving the weak formulation of Eq. (7) as

$$\int_{a}^{b} \left(u(t)\dot{\phi}(t) + f(u(t), t; \theta)\phi(t) \right) dt = 0, \tag{8}$$

which avoids estimating $\dot{u}(t)$ from noisy data u(t).

Subdomain Decomposition. To enhance flexibility and enable localized modeling, we employ the weak formulation to K overlapping subdomains that cover the time domain of the available training time series. Each subdomain is mapped from the physical time coordinate $t \in [a_k, b_k]$ to a local reference coordinate $s \in [-1, 1]$ via a standard affine transformation $t = \tau_k(s) := \frac{b_k - a_k}{2} s + \frac{a_k + b_k}{2}$. Each subdomain contains M uniformly spaced grid points (spacing Δt).

Weak Form Test Functions. The choice of test functions is critical for the accuracy and efficiency of weakform integration. Following [49], we adopt the even polynomial family on the reference domain [-1, 1],

$$\phi_p(s) = (1 - s^2)^p, \quad s \in [-1, 1], \ p \in \mathbb{N}.$$
 (9)

This construction ensures vanishing at the boundaries $(\phi_p(\pm 1) = 0)$, allows smoothness to be tuned by the integer p, and, being polynomial, permits semi-analytical evaluation of the weak-form integrals. Detailed derivations are provided in the *Supplementary Note 5*.

Reference Mapping. Using the affine map $t=\tau_k(s)$, we have $ds=\frac{2}{L}\,dt$. Hence, $\frac{d\phi}{dt}=\frac{d\phi}{ds}\frac{ds}{dt}=\dot{\phi}(s)\frac{2}{L}$. The terms in the weak form from Eq. (8) transform as

$$\int u(t)\dot{\phi}(t)dt = \int_{-1}^{1} u(\tau_k(s))\dot{\phi}(s)ds,$$
$$\int f(u(t),t;\theta)\phi(t)dt = \int_{-1}^{1} f(u(\tau_k(s)),\tau_k(s);\theta)\phi(s)\frac{L}{2}ds.$$

where $L = (M-1)\Delta t$ is the subdomain length. Overall, this localized formulation enables accurate and efficient evaluation of the weak residual within each subdomain using compactly supported test functions on [-1,1].

Weak Form Loss and Vectorization. To evaluate the weak form in practice, we represent both the data u(s) and the function evaluations $f(u(s), s; \theta)$ using piecewise linear interpolation between M grid points on each subdomain. This allows the weak form integrals to be expressed as linear combinations of the nodal values u_i and the neural network evaluations at those nodes $f_i := f(u_i, t_i; \theta)$. Particularly,

$$\int u(\tau_k(s))\dot{\phi}(s)ds \approx \sum_{i=0}^{M-1} u_i w_{\text{lhs},i} = \mathbf{u}^{\top} \mathbf{w}_{\text{lhs}},$$

$$\int f(u(\tau_k(s)), \tau_k(s); \theta) \phi(s) \frac{L}{2} ds \approx \sum_{i=0}^{M-1} f_i w_{\text{rhs},i} = \mathbf{f}^{\top} \mathbf{w}_{\text{rhs}},$$

where the precomputable weights are $w_{\text{lhs},i} = \int \ell_i(s)\dot{\phi}(s)ds$ and $w_{\text{rhs},i} = \frac{L}{2}\int \ell_i(s)\phi(s)ds$. Here, $\ell_i(s)$ denotes the linear Lagrange basis function centered at the grid point x_i .

Since ϕ is smooth and $\ell_i(s)$ is linear, the weights admit exact closed-form expressions. In vectorized form, the weak-form loss is defined as the squared residual:

$$\mathcal{L}_{\text{weak}}(\theta) = \left\| \mathbf{u}^{\top} \mathbf{w}_{\text{lhs}} + \mathbf{f}^{\top} \mathbf{w}_{\text{rhs}} \right\|^{2}, \tag{10}$$

where **f** denotes the vector of neural network evaluations at the nodal points **u** in each subdomain, i.e., **f** = $[f(u_0, t_0; \theta), f(u_1, t_1; \theta), \dots, f(u_{M-1}, t_{M-1}; \theta)]^{\top}$. This formulation naturally generalizes to higher-dimensional or vector-valued data via batched dot products across dimensions. Detailed derivations, including the piecewise linear interpolation, the explicit form of the basis functions $\ell_i(s)$, and the construction of the weights, are

provided in the Supplementary Note 6.

WP-NODE Loss Function. To leverage the complementary strengths of strong-form and weak-form supervision, WP-NODE is trained using a weak penalty added to the standard strong-form loss. The total loss is formulated as a weighted combination of Eq. (6) and Eq. (10), balancing pointwise accuracy with integrated residual consistency.

$$\mathcal{L} = \mathcal{L}_{\text{weak}} + \lambda \mathcal{L}_{\text{strong}}, \tag{11}$$

where λ is a regularization coefficient balancing the two components.

A key distinction in our implementation is that $\mathcal{L}_{\mathrm{strong}}$ is computed using significantly shorter forward-simulation rollouts (typically with $1 \leq T \leq 5$) compared to standalone strong-form approaches. This design reflects a complementary role between the two loss components: The weak-form loss shapes the model's global behavior via integral residuals while mitigating noise, whereas the strong-form loss provides a direct, localized supervisory signal. Such exposure to the true temporal evolution reinforces correct local dynamics, enhancing predictive fidelity without the cost or instability of long-horizon rollouts.

Dataset and Training. Training samples were generated using a sliding-window approach, where each windowed segment defines a short trajectory of fixed length, enabling consistent training across strong, weak, and WP-NODE formulations. Data is scaled using a Min-Max scaler fitted on the training data. For the L63, L96, and KS systems, shallow neural networks with one or two layers and GELU activations were employed and trained with the Adam optimizer. A CNN was used to model the multidimensional ERA5 dataset. A learning rate scheduler and early stopping based on validation loss are applied to ensure efficient convergence. For inference and reference solution generation, the adaptive dopri5 solver is employed in double precision with a strict numerical tolerance. For the ERA5 data, a simple Euler step is used. Full details on all hyperparameters (e.g., subdomain sizes, batch sizes, learning rates, etc.) and other configurations are provided in Supplementary Note 4 and 7.

Acknowledgments This research used resources of the National Energy Research Scientific Computing Center (NERSC), a U.S. Department of Energy Office of Science User Facility, and the Institute for Computational and Data Sciences (ICDS) at Pennsylvania State University. R.M. acknowledges support from the U.S. Army Research Office (ARO) Young Investigator Program under the Multiscale Modeling of Complex Systems, PM - Rob Martin. The research of J.H. was partially supported by the NSF Grant DMS-2505605 and the Office of Naval Research (ONR) grant N000142212193.

Author contributions J.H. and R.M. supervised the

study. X.L., J.H., and R.M. contributed to the initial concept and machine learning methodology. X.L. carried out model development, implementation, training, and analysis. D.C. contributed to the EAR5 dataset processing, training, and visualization. All authors contributed to writing the manuscript.

Competing interests The authors declare no competing interests.

- * Corresponding author: xuyang.li@charlotte.edu
 † Corresponding author: rmaulik@psu.edu
- A. Ghadami and B. I. Epureanu, Data-driven prediction in dynamical systems: recent developments, Philosophical Transactions of the Royal Society A 380, 20210213 (2022).
- [2] F. Morrison, The art of modeling dynamic systems: forecasting for chaos, randomness and determinism (Courier Corporation, 2012).
- [3] K. Kaheman, E. Kaiser, B. Strom, J. N. Kutz, and S. L. Brunton, Learning discrepancy models from experimental data, arXiv preprint arXiv:1909.08574 (2019).
- [4] J. Hart, S. A. McQuarrie, Z. Morrow, and B. v. B. Waanders, Toward real-time optimization through model reduction and model discrepancy sensitivities, arXiv preprint arXiv:2508.21792 (2025).
- [5] S. L. Brunton and J. N. Kutz, Data-driven science and engineering: Machine learning, dynamical systems, and control (Cambridge University Press, 2022).
- [6] R. Wang, D. Maddix, C. Faloutsos, Y. Wang, and R. Yu, Bridging physics-based and data-driven modeling for learning dynamical systems, in *Learning for dynamics* and control (PMLR, 2021) pp. 385–398.
- [7] D. Floryan and M. D. Graham, Data-driven discovery of intrinsic dynamics, Nature Machine Intelligence 4, 1113 (2022).
- [8] M. J. Colbrook and A. Townsend, Rigorous data-driven computation of spectral properties of koopman operators for dynamical systems, Communications on Pure and Applied Mathematics 77, 221 (2024).
- [9] A. A. Kaptanoglu, J. L. Callaham, A. Aravkin, C. J. Hansen, and S. L. Brunton, Promoting global stability in data-driven models of quadratic nonlinear dynamics, Physical Review Fluids 6, 094401 (2021).
- [10] C. Legaard, T. Schranz, G. Schweiger, J. Drgoňa, B. Falay, C. Gomes, A. Iosifidis, M. Abkar, and P. Larsen, Constructing neural network based models for simulating dynamical systems, ACM Computing Surveys 55, 1 (2023).
- [11] W. Gilpin, Chaos as an interpretable benchmark for forecasting and data-driven modelling, arXiv preprint arXiv:2110.05266 (2021).
- [12] M. Levine and A. Stuart, A framework for machine learning of model error in dynamical systems, Communications of the American Mathematical Society 2, 283 (2022).
- [13] D. E. Rumelhart, G. E. Hinton, and R. J. Williams, Learning representations by back-propagating errors, nature 323, 533 (1986).
- [14] A. Chattopadhyay, P. Hassanzadeh, and D. Subrama-

- nian, Data-driven prediction of a multi-scale lorenz 96 chaotic system using deep learning methods: Reservoir computing, ann, and rnn-lstm, Nonlinear Processes in Geophysics Discussions **2020**, 1 (2020).
- [15] S. Hochreiter and J. Schmidhuber, Long short-term memory, Neural computation 9, 1735 (1997).
- [16] J. Harlim, S. W. Jiang, S. Liang, and H. Yang, Machine learning for prediction with missing dynamics, Journal of Computational Physics 428, 109922 (2021).
- [17] M. U. Kobayashi, K. Nakai, Y. Saiki, and N. Tsutsumi, Dynamical system analysis of a data-driven model constructed by reservoir computing, Physical Review E 104, 044215 (2021).
- [18] M. Yan, C. Huang, P. Bienstman, P. Tino, W. Lin, and J. Sun, Emerging opportunities and challenges for the future of reservoir computing, Nature Communications 15, 2056 (2024).
- [19] F. M. Bianchi, S. Scardapane, S. Løkse, and R. Jenssen, Reservoir computing approaches for representation and classification of multivariate time series, IEEE transactions on neural networks and learning systems 32, 2169 (2020).
- [20] C. Lea, R. Vidal, A. Reiter, and G. D. Hager, Temporal convolutional networks: A unified approach to action segmentation, in *European conference on computer vision* (Springer, 2016) pp. 47–54.
- [21] V. Perumal, D. Abueidda, S. Koric, and A. Kontsos, Temporal convolutional networks for data-driven thermal modeling of directed energy deposition, Journal of Manufacturing Processes 85, 405 (2023).
- [22] A. Vaswani, N. Shazeer, N. Parmar, J. Uszkoreit, L. Jones, A. N. Gomez, L. Kaiser, and I. Polosukhin, Attention is all you need, Advances in neural information processing systems 30 (2017).
- [23] Y. He, Y. Yang, X. Cheng, H. Wang, X. Xue, B. Chen, and Y. Hu, Chaos meets attention: Transformers for large-scale dynamical prediction, arXiv preprint arXiv:2504.20858 (2025).
- [24] A. Patil, J. Viquerat, and E. Hachem, Autoregressive transformers for data-driven spatiotemporal learning of turbulent flows, APL Machine Learning 1 (2023).
- [25] P. Mandal and G. A. Gottwald, Learning dynamical systems with hit-and-run random feature maps, Nature Communications 16, 5961 (2025).
- [26] R. T. Chen, Y. Rubanova, J. Bettencourt, and D. K. Duvenaud, Neural ordinary differential equations, Advances in neural information processing systems 31 (2018).
- [27] Y. Oh, S. Kam, J. Lee, D.-Y. Lim, S. Kim, and A. Bui, Comprehensive review of neural differential equations for time series analysis, arXiv preprint arXiv:2502.09885 (2025).
- [28] P. Kidger, On neural differential equations, arXiv preprint arXiv:2202.02435 (2022).
- [29] O. Ronneberger, P. Fischer, and T. Brox, U-net: Convolutional networks for biomedical image segmentation, in *International Conference on Medical image computing and computer-assisted intervention* (Springer, 2015) pp. 234–241.
- [30] C. Rackauckas, Y. Ma, J. Martensen, C. Warner, K. Zubov, R. Supekar, D. Skinner, A. Ramadhan, and A. Edelman, Universal differential equations for scientific machine learning, arXiv preprint arXiv:2001.04385 (2020).
- [31] Y. Ma, V. Dixit, M. J. Innes, X. Guo, and C. Rack-

- auckas, A comparison of automatic differentiation and continuous sensitivity analysis for derivatives of differential equation solutions, in 2021 IEEE High Performance Extreme Computing Conference (HPEC) (IEEE, 2021) pp. 1–9.
- [32] D. Chakraborty, S. W. Chung, T. Arcomano, and R. Maulik, Divide and conquer: Learning chaotic dynamical systems with multistep penalty neural ordinary differential equations, Computer Methods in Applied Mechanics and Engineering 432, 117442 (2024).
- [33] D. Chakraborty, S. W. Chung, A. Chattopadhyay, and R. Maulik, Improved deep learning of chaotic dynamical systems with multistep penalty losses, arXiv preprint arXiv:2410.05572 (2024).
- [34] A. Allauzen, T. P. M. Dardis, and H. Plath, Experimental study of neural ode training with adaptive solver for dynamical systems modeling, arXiv preprint arXiv:2211.06972 (2022).
- [35] A. J. Linot, J. W. Burby, Q. Tang, P. Balaprakash, M. D. Graham, and R. Maulik, Stabilized neural ordinary differential equations for long-time forecasting of dynamical systems, Journal of Computational Physics 474, 111838 (2023).
- [36] C. Fronk and L. Petzold, Training stiff neural ordinary differential equations with explicit rational taylor series methods, Chaos: An Interdisciplinary Journal of Nonlinear Science 35 (2025).
- [37] C. Fronk and L. Petzold, Training stiff neural ordinary differential equations with implicit single-step methods, Chaos: An Interdisciplinary Journal of Nonlinear Science 34 (2024).
- [38] S. Cheng, C. Quilodrán-Casas, S. Ouala, A. Farchi, C. Liu, P. Tandeo, R. Fablet, D. Lucor, B. Iooss, J. Brajard, et al., Machine learning with data assimilation and uncertainty quantification for dynamical systems: a review, IEEE/CAA Journal of Automatica Sinica 10, 1361 (2023).
- [39] S. Mukhopadhyay and S. Banerjee, Learning dynamical systems in noise using convolutional neural networks, Chaos: An Interdisciplinary Journal of Nonlinear Science 30 (2020).
- [40] D. A. Messenger and D. M. Bortz, Weak sindy for partial differential equations, Journal of Computational Physics 443, 110525 (2021).
- [41] J. Hsin, S. Agarwal, A. Thorpe, L. Sentis, and D. Fridovich-Keil, Symbolic regression on sparse and noisy data with gaussian processes, in 2025 American Control Conference (ACC) (IEEE, 2025) pp. 3170–3175.
- [42] S. Yang, S. W. Wong, and S. Kou, Inference of dynamic systems from noisy and sparse data via manifold-constrained gaussian processes, Proceedings of the National Academy of Sciences 118, e2020397118 (2021).
- [43] O. Stegle, S. V. Fallert, D. J. MacKay, and S. Brage, Gaussian process robust regression for noisy heart rate data, IEEE Transactions on Biomedical Engineering 55, 2143 (2008).
- [44] A. Seleznev, D. Mukhin, A. Gavrilov, E. Loskutov, and A. Feigin, Bayesian framework for simulation of dynamical systems from multidimensional data using recurrent neural network, Chaos: An Interdisciplinary Journal of Nonlinear Science 29 (2019).
- [45] L. Yang, X. Meng, and G. E. Karniadakis, B-pinns: Bayesian physics-informed neural networks for forward and inverse pde problems with noisy data, Journal of

- Computational Physics **425**, 109913 (2021).
- [46] Z. Guo, I. Cialenco, and M. Zhong, Learning stochastic dynamics from data, arXiv preprint arXiv:2403.02595 (2024).
- [47] L. Ding and C. Wen, High-order extended kalman filter for state estimation of nonlinear systems, Symmetry 16, 617 (2024).
- [48] R. Stephany and C. Earls, Weak-pde-learn: A weak form based approach to discovering pdes from noisy, limited data, Journal of Computational Physics 506, 112950 (2024).
- [49] D. M. Bortz, D. A. Messenger, and A. Tran, Weak form-based data-driven modeling: Computationally efficient and noise robust equation learning and parameter inference, in *Handbook of Numerical Analysis*, Vol. 25 (Elsevier, 2024) pp. 53–82.
- [50] N. Rummel, D. A. Messenger, S. Becker, V. Dukic, and D. M. Bortz, Wendy for nonlinear-in-parameters odes, arXiv preprint arXiv:2502.08881 (2025).
- [51] T. De Ryck, S. Mishra, and R. Molinaro, wpinns: Weak physics informed neural networks for approximating entropy solutions of hyperbolic conservation laws, SIAM Journal on Numerical Analysis 62, 811 (2024).
- [52] E. Kharazmi, Z. Zhang, and G. E. Karniadakis, hp-vpinns: Variational physics-informed neural networks with domain decomposition, Computer Methods in Applied Mechanics and Engineering 374, 113547 (2021).
- [53] D. A. Messenger and D. M. Bortz, Weak sindy: Galerkin-based data-driven model selection, Multiscale Modeling & Simulation 19, 1474 (2021).
- [54] H. Zhao, Y. Wang, H. Qi, Z. Huang, H. Zhao, L. Sha, and H. Shao, Accelerating neural odes: A variational formulation-based approach, in *The Thirteenth Interna*tional Conference on Learning Representations (2025).
- [55] S. Kullback and R. A. Leibler, On information and sufficiency, The annals of mathematical statistics 22, 79 (1951).
- [56] E. N. Lorenz, Deterministic nonperiodic flow 1, in *Universality in Chaos*, 2nd edition (Routledge, 2017) pp. 367–378
- [57] E. N. Lorenz, Predictability: A problem partly solved, in Proc. Seminar on predictability, Vol. 1 (Readinhig, 1996) pp. 1–18
- [58] R. A. Edson, J. E. Bunder, T. W. Mattner, and A. J. Roberts, Lyapunov exponents of the kuramotosivashinsky pde, The ANZIAM Journal 61, 270 (2019).
- [59] H. Fan, J. Jiang, C. Zhang, X. Wang, and Y.-C. Lai, Long-term prediction of chaotic systems with machine learning, Physical Review Research 2, 012080 (2020).
- [60] H. Hersbach, B. Bell, P. Berrisford, S. Hirahara, A. Horányi, J. Muñoz-Sabater, J. Nicolas, C. Peubey, R. Radu, D. Schepers, et al., The era5 global reanalysis, Quarterly journal of the royal meteorological society 146, 1999 (2020).
- [61] T. Arcomano, I. Szunyogh, A. Wikner, J. Pathak, B. R. Hunt, and E. Ott, A hybrid approach to atmospheric modeling that combines machine learning with a physicsbased numerical model, Journal of Advances in Modeling Earth Systems 14, e2021MS002712 (2022).
- [62] H. Guan, T. Arcomano, A. Chattopadhyay, and R. Maulik, Lucie: A lightweight uncoupled climate emulator with long-term stability and physical consistency for o (1000)-member ensembles, arXiv preprint arXiv:2405.16297 (2024).

- [63] J. R. Dormand and P. J. Prince, A family of embedded runge-kutta formulae, Journal of computational and applied mathematics **6**, 19 (1980).
- [64] J. C. Butcher, Numerical methods for ordinary differential equations (John Wiley & Sons, 2016).

Supplementary Information

SUPPLEMENTARY NOTE 1: LORENZ 63 INVARIANT MEASURE ANALYSIS

To complement the quantitative KL divergence results presented in Table 1 of the article, this note provides a detailed visual comparison of the predicted and ground-truth PDFs for the L63 system under different modeling approaches. These comparisons offer a more intuitive understanding of how well each method captures the system's invariant measure, especially under various noise levels.

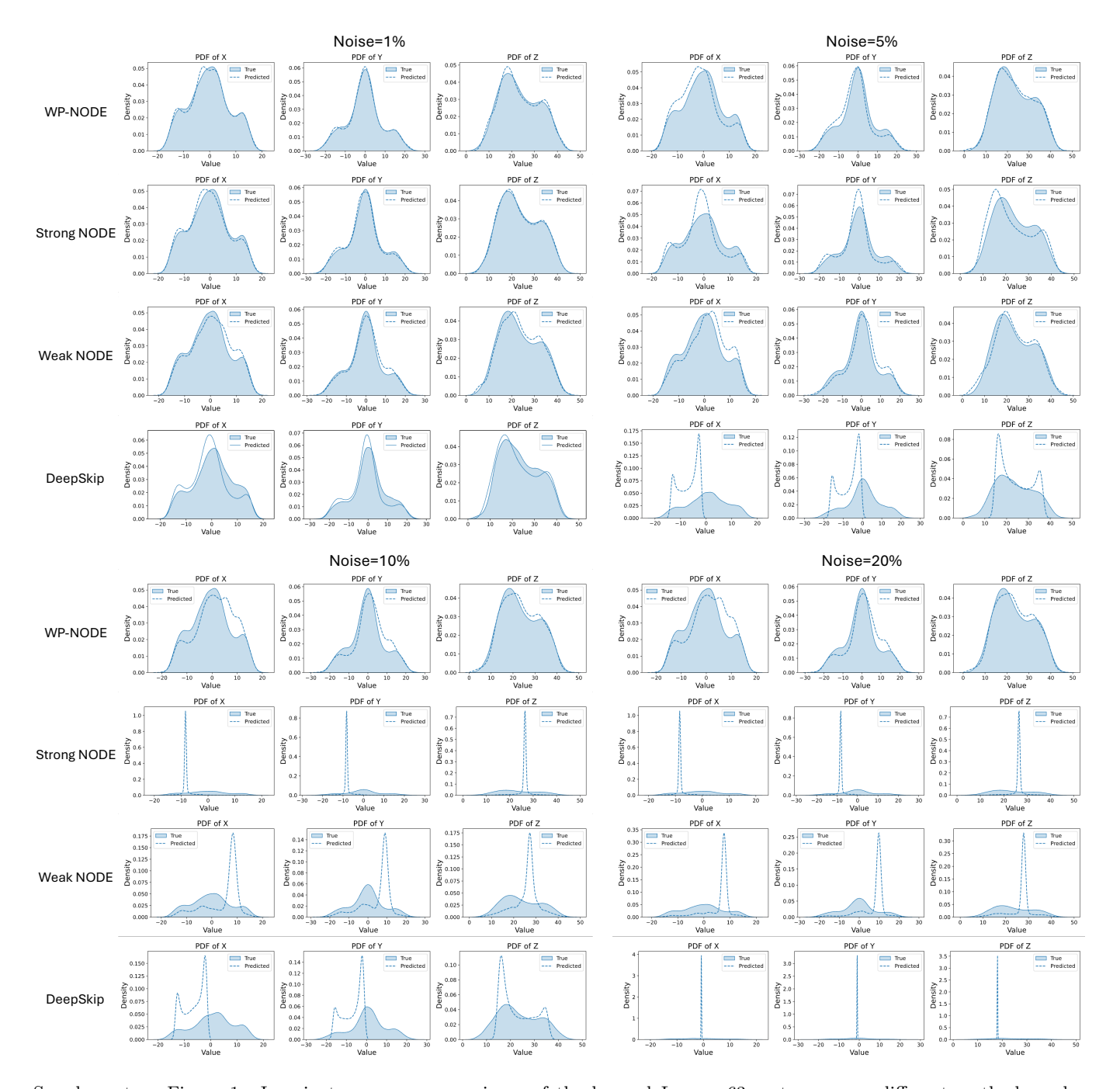
As shown in Supplementary Fig. 1, each row corresponds to a different modeling approach (WP-NODE, strong NODE, weak NODE, and DeepSkip), and the columns show the estimated PDFs for the x, y, and z state variables under 1%, 5%, 10%, and 20% noise levels. Overall, as the noise level increases, the mismatch between the predicted and true distributions becomes more significant for all methods. Notably, under 10% and 20% noise, both the weak and strong NODE struggle to recover meaningful distributions, often collapsing toward narrow or overly concentrated profiles that deviate substantially from the true attractor. In contrast, the proposed method continues to produce PDFs that closely resemble the ground truth across all state dimensions, demonstrating strong robustness in preserving long-term statistical structure even in highly noisy conditions.

These results reinforce the KL divergence findings and further highlight the advantage of the proposed method in capturing the correct invariant measure under real-world noise.

SUPPLEMENTARY NOTE 2: ABLATION STUDY

A comprehensive ablation analysis was performed to investigate the influence of key hyperparameters. The default configuration consists of a two-layer neural network with 200 neurons per layer, subdomain size M=60, training signal length of 100s, batch size of 1024, and number of subdomains K=5000 (half of the total sample size N). The polynomial order of the test function is p=16, the number of rollout trajectories is set to 1, and the regularization coefficient $\lambda=0.5$ balances the weak- and strong-form losses.

In Supplementary Fig. 2, each hyperparameter is varied individually while keeping all others fixed. Model performance is evaluated using the VPT and KL divergence metrics. As illustrated in Supplementary Fig. 2a, increasing the number of hidden layers leads to a noticeable degradation in performance. This counterintuitive trend likely arises from the higher sensitivity of deeper networks to input perturbations, making them more difficult to train under noisy conditions. Additional tests (not shown) conducted at higher noise levels further confirm that shallower architectures (e.g., single-layer networks) consistently outperform deeper ones. In Supplementary Fig. 2b, the effect of the integration subdomain size M does not exhibit a clear optimum. Larger subdomains generally enhance numerical stability but reduce local adaptivity, whereas smaller ones capture finer local structures at the expense of stability.

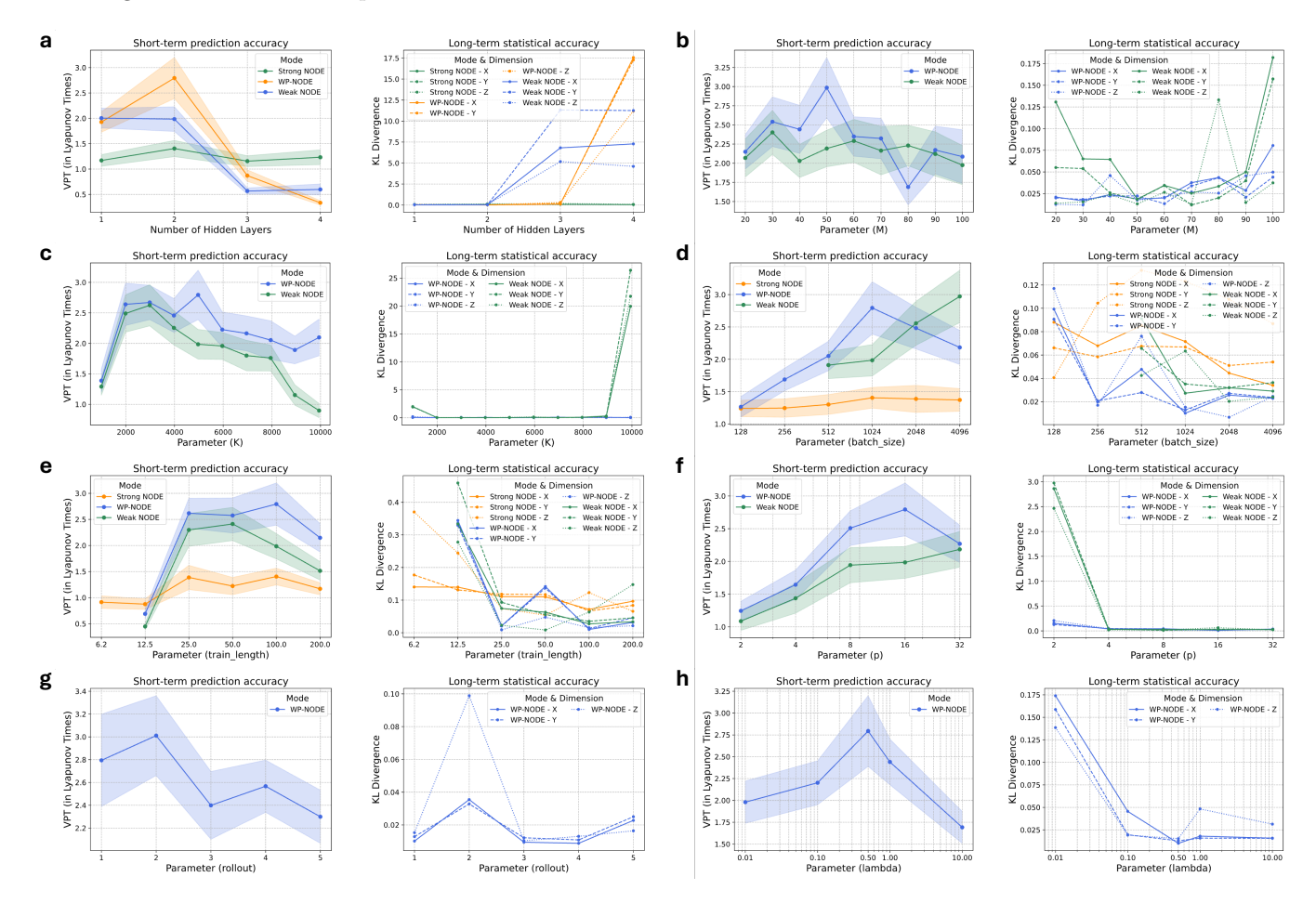


Supplementary Figure 1. Invariant measure comparisons of the learned Lorenz–63 system across different methods under varying noise conditions.

In Supplementary Fig. 2c, the weak NODE and WP-NODE maintain high VPT scores even with substantially shorter training signals. For instance, accurate short-time prediction performance is achieved with training signals as short as 12.5s, indicating that minimal temporal information is sufficient to capture the system's essential dynamics under these formulations. In Supplementary Fig. 2d, batch size plays a critical role in training stability. Smaller batches often lead to unstable learning and divergent dynamics during inference, occasionally causing integration failures due to exploding values. Larger batch sizes, in contrast, stabilize optimization and improve generalization.

In Supplementary Fig. 2e, the model performance varies with the number of subdomains K. Intermediate values, typically around half of the total samples (e.g., K = 5000 when $K_{\text{total}} = 10000$), yield the best balance between short-term prediction accuracy and long-term statistical stability. This configuration is therefore adopted as the default setting in the experiments for the other two chaotic systems, L96 and KS. In Supplementary Fig. 2f, the polynomial order p of the test function strongly influences weak-form integration accuracy. Values around p = 16 yield optimal performance, likely due to the balanced smoothness and localization of the basis functions.

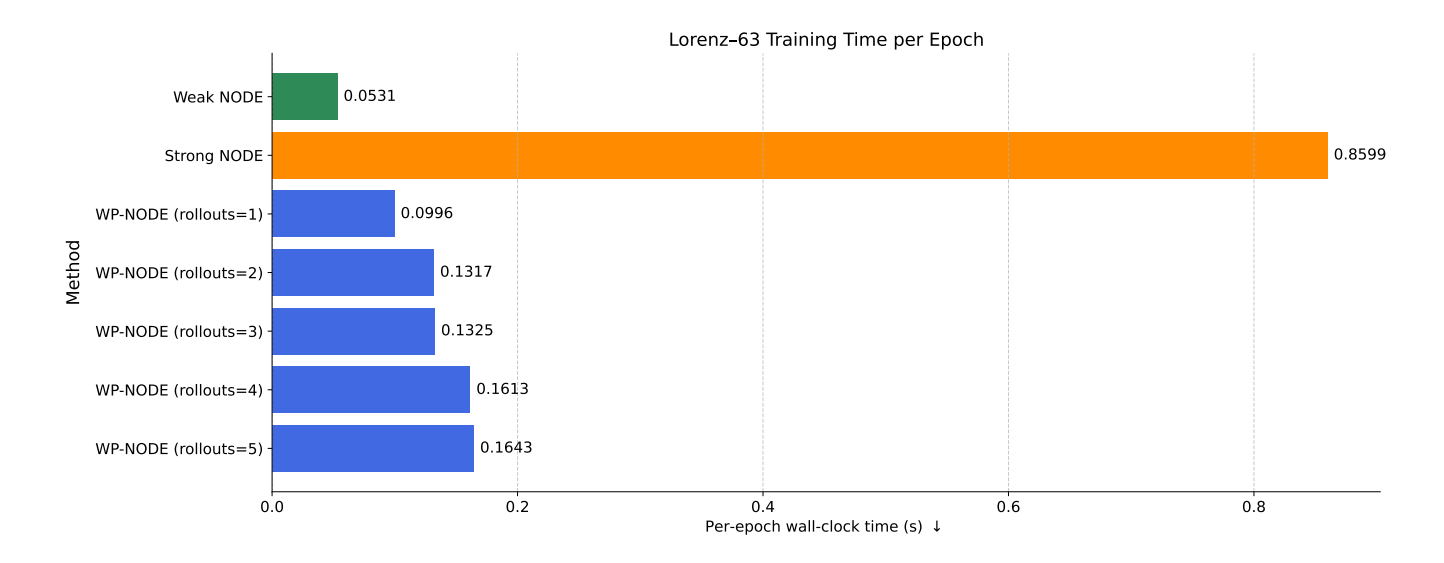
Notably, Supplementary Fig. 2g shows that increasing the number of rollouts in WP-NODE enhances pointwise residual minimization and temporal consistency. However, higher rollout counts also increase computational cost, highlighting a trade-off between accuracy and efficiency. Lastly, in Supplementary Fig. 2h, the regularization coefficient λ critically affects performance. Moderate values (e.g., $\lambda = 0.5$) balance weak-form integration and pointwise errors, achieving the best short-term performance.



Supplementary Figure 2. Comprehensive ablation study of the learned L63 system. **a.** Number of hidden layers, each layer has 200 neurons. **b.** The integration domain size M. **c.** The training signal length in seconds. **d.** The batch size during training. **e.** The number of subdomains K. **f.** The polynomial order p of the test function. **g.** The number of rollouts used in WP-NODE for pointwise residual minimization. **h.** The regularization coefficient λ balances the loss from weak and strong formulations.

In Supplementary Fig. 3, the per-epoch training time of WP-NODE remains close to that of the weak NODE, while being significantly faster than the strong NODE, which uses 25 rollouts across all systems. Specifically, WP-NODE

with a single rollout requires only 0.10 seconds per epoch, approximately $8.6 \times$ faster than the strong formulation, while additional rollouts (≤ 5) increase the cost modestly to about 0.16 seconds per epoch. This confirms that WP-NODE achieves an excellent balance between computational efficiency and temporal accuracy: it preserves the stability benefits of strong supervision without incurring its high computational burden.



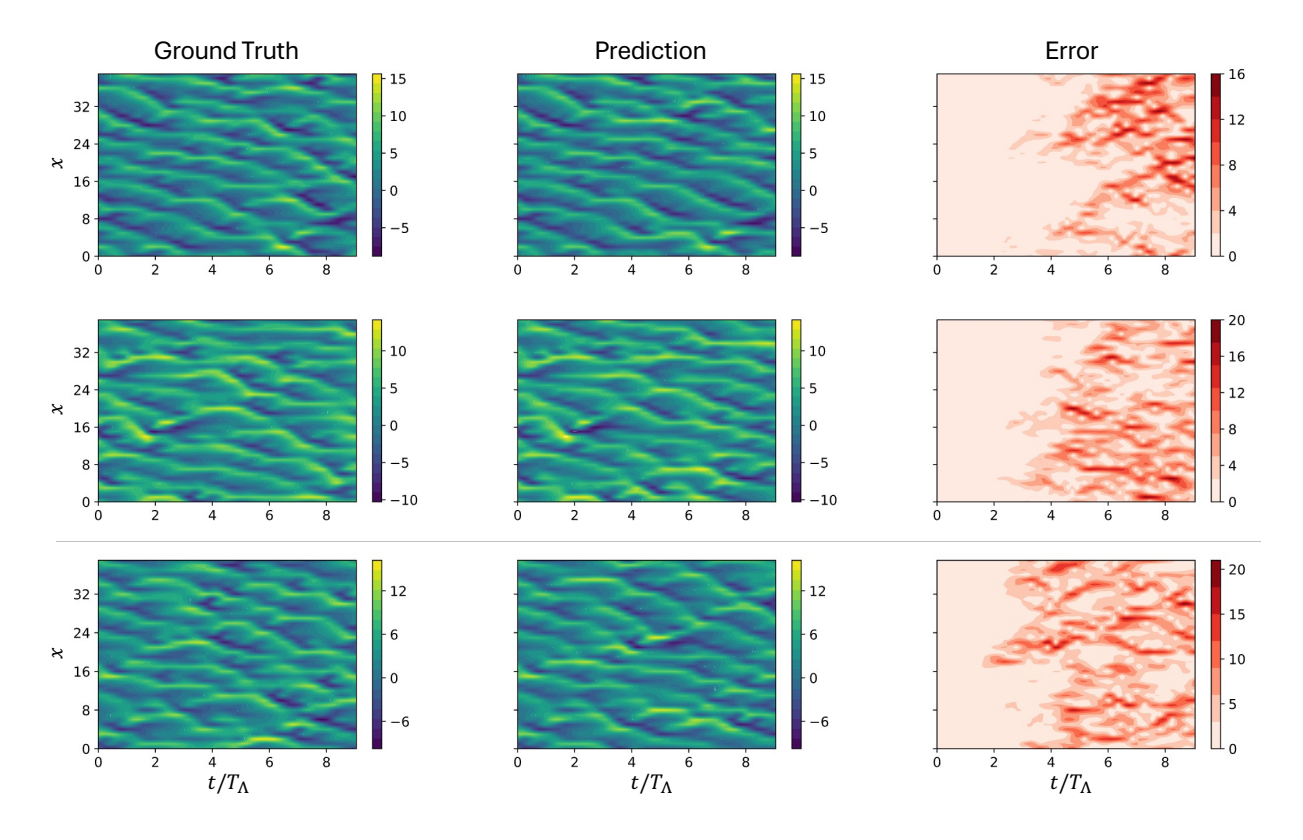
Supplementary Figure 3. Per-epoch wall-clock time (in seconds) for training different models on the L63 system. WP-NODE is shown with varying rollouts, from 1 to 5. The strong NODE uses 25 rollouts. All models use a 2-layer network architecture with 200 hidden neurons. Lower times indicate faster training.

SUPPLEMENTARY NOTE 3: LORENZ 96 ANALYSIS

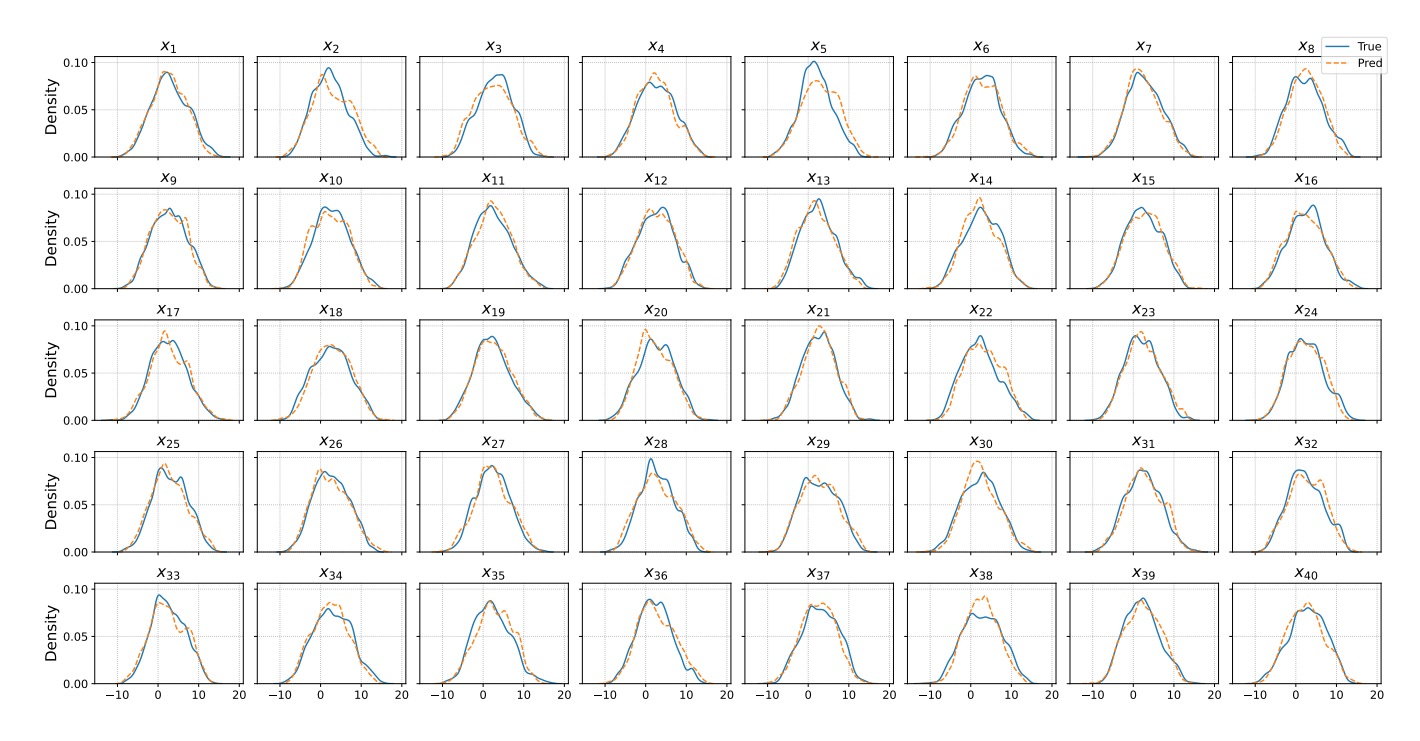
Since all methods exhibit broadly similar performance on the L96 system, with WP-NODE showing only a modest improvement in both predictive accuracy and statistical consistency, only its results are presented here for clarity.

Supplementary Fig. 4 illustrates the extrapolation performance of WP-NODE on the 40-dimensional L96 system under 5% observational noise. The three rows correspond to different initial conditions, representing the best, average, and worst cases, with VPT scores of 4.29, 3.31, and 1.97, respectively. Across all cases, WP-NODE accurately reproduces the dominant spatiotemporal structures and maintains phase coherence over multiple Lyapunov times.

Supplementary Fig. 5 compares the invariant measures of the learned and reference systems across all 40 dimensions. The predicted distributions closely align with the ground truth, confirming that WP-NODE not only yields stable short-term forecasts but also preserves the long-term statistical equilibrium of the system. The slight deviations in a few components likely stem from high-dimensional mixing and the limited discriminative sensitivity of one-dimensional marginal densities. Overall, WP-NODE ensures stable extrapolation and accurate recovery of statistical properties, even in high-dimensional chaotic dynamics.



Supplementary Figure 4. Forecasting of the Lorenz–96 system using WP-NODE under 5% training data noise. The three rows correspond to three different initial conditions for extrapolation, representing the best, average, and worst cases. From top to bottom, the VPT scores are 4.29, 3.31, and 1.97.



Supplementary Figure 5. Invariant measures of the learned Lorenz–96 system using WP-NODE under 5% training data noise. The 40 dimensions are presented respectively.

SUPPLEMENTARY NOTE 4: ERA5 ANALYSIS

The ERA5 dataset was subjected to min-max normalization, and the data were partitioned chronologically into training and validation sets. The training set contains 11,576 samples that span approximately 7.9 years of data. The validation and test sets contain 4,920 samples that cover the remaining period. Model development and model selection were performed using only the training and validation sets.

The NODE for modeling the ERA5 does not use a simple feed-forward network to parameterize the right-hand side. Instead, the derivative function is implemented by a structured architecture composed of three components in sequence. The encoder compresses the input state and conditioning variables into a latent representation. This latent representation is then processed by multiple residual blocks in the dilated CNN processor, with each block applying a sequence of dilated convolutions to capture multi-scale patterns. Finally, the decoder maps the processed latent representation back to physical space, producing the rate of change for each predicted variable. To correctly model the Earth's spherical shape, all convolutional operations use cylindrical boundary conditions: circular padding for longitude (to connect East and West) and replicate padding for latitude (to handle the poles).

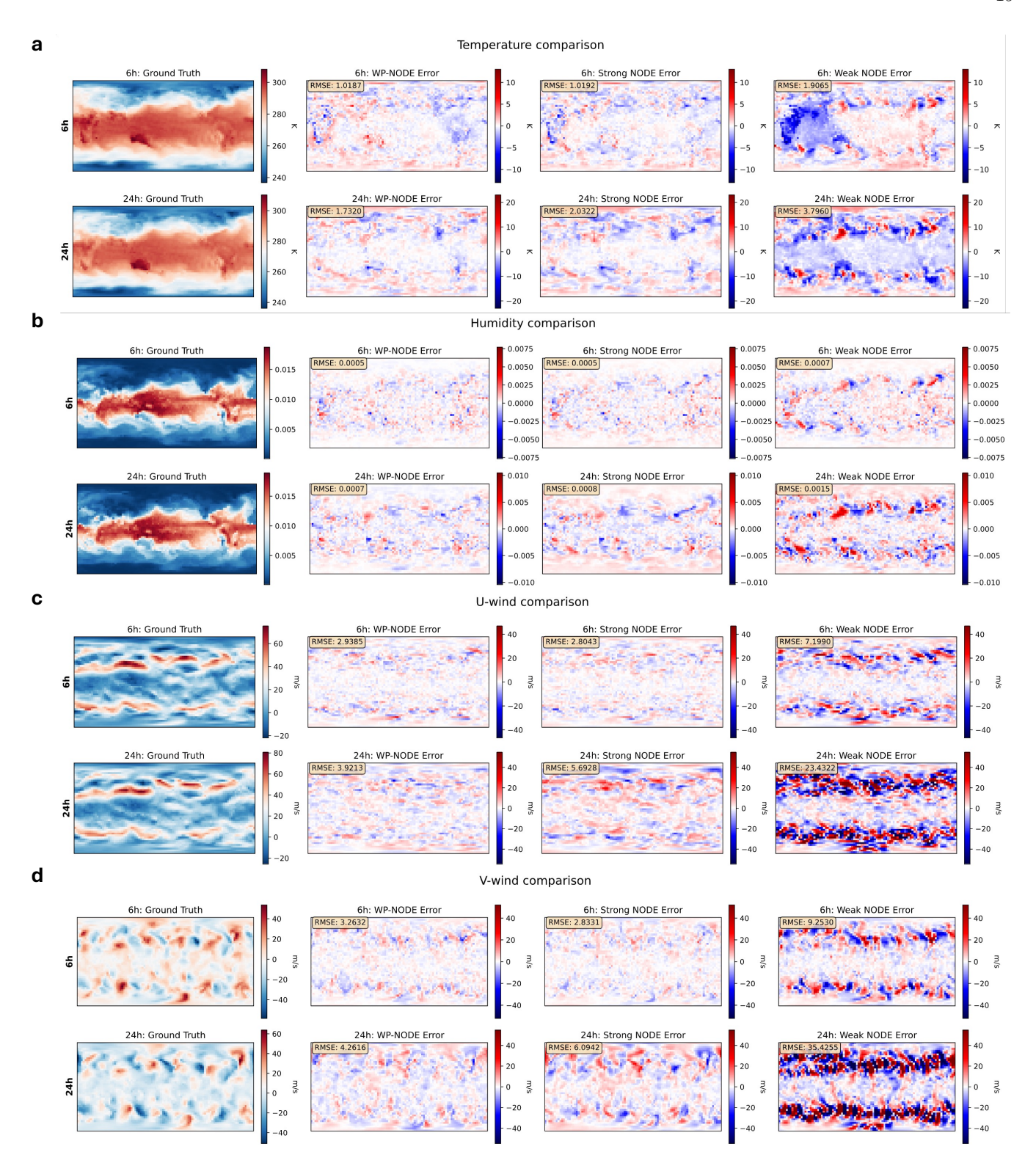
Since solar forcing varies with time and location, our NODE model accepts conditioning information as an additional input. The temporal integration is performed using the Euler method:

$$x_{t+1} = x_t + f(x_t, u_t, t; \theta) \Delta t, \tag{S1}$$

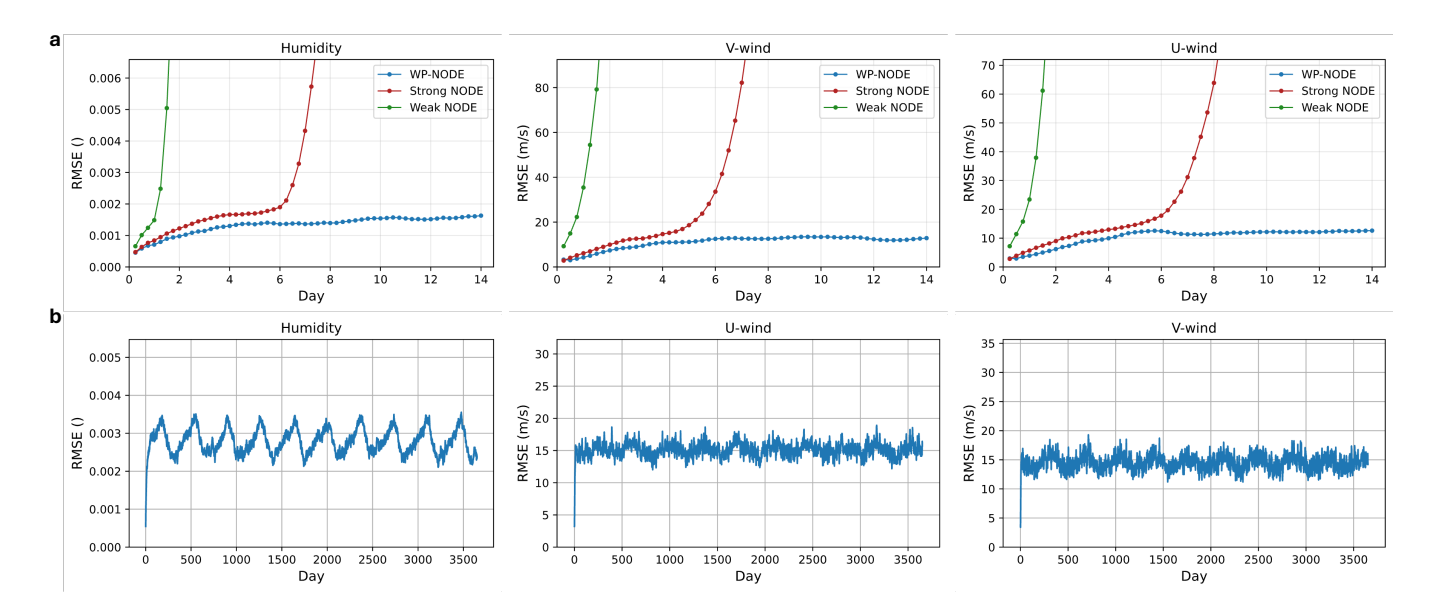
where x_t represents the atmospheric state, u_t is the time-dependent input forcing (i.e., solar radiation), θ denotes the learnable parameters, and Δt is the integration time step. The time variable is non-dimensionalized by the data sampling interval (6 hours). Therefore, the integration step size is set to $\Delta t = 1$ in the discrete model, representing one step of forward prediction corresponding to a 6-hour physical duration. During training, the strong NODE employs 6 rollout steps, while the weak NODE uses a subdomain size of 8. WP-NODE loss combines both settings above with the penalty $\lambda = 1$.

In Fig. 6, short-term predictions from WP-NODE are compared with two baseline NODE models for 6-hour and 24-hour forecasts across the four prognostic variables. WP-NODE consistently outperforms both baselines across all variables and time horizons.

In Fig. 7a, the 14-day RMSE evolution is shown for the three prognostic variables not included in the main article (the temperature variable was presented in the main text). The weak and strong baseline NODE models diverge and produce unstable predictions within days, while WP-NODE maintains stable and accurate forecasts throughout the 14-day period. Fig. 7b further demonstrates that WP-NODE can maintain forecast stability over significantly longer time horizons. These results further strengthen the claims in the main article that WP-NODE's hybrid training strategy delivers superior stability, accuracy, and long-term predictive fidelity in real-world climate forecasting, precisely where



Supplementary Figure 6. Short-term prediction comparison (using RMSE) on the ERA5 dataset over the four prognostic variables. a. Temperature. b. Humidity. c. Zonal component of the horizontal wind velocity. d. Meridional component of the horizontal wind velocity.



Supplementary Figure 7. Long-term prediction comparison (using RMSE) on the ERA5 dataset over the other three prognostic variables (i.e., humidity, zonal, and meridional component of the horizontal wind velocity. **a**. Comparisons of 14-day predictions. **b**. 1-year prediction performance of WP-NODE.

SUPPLEMENTARY NOTE 5: POLYNOMIAL TEST FUNCTIONS

This note provides the explicit derivative expansions, antiderivatives, and weight constructions for the polynomial test functions $\phi_p(s) = (1 - s^2)^p$ used in the weak-form integration. These functions vanish at the subdomain boundaries, $\phi_p(\pm 1) = 0$, which makes them particularly well-suited for localized formulations.

The $d^{\rm th}$ derivative of ϕ_p admits the closed-form expansion

$$\phi_p^{(d)}(s) = \sum_{k=0}^p (-1)^k \binom{p}{k} \frac{(2p-2k)!}{(2p-2k-d)!} s^{2(p-k)-d}.$$

Since $\phi_p^{(d)}(s)$ and $s\phi_p^{(d)}(s)$ are polynomials, their primitives also have closed-form expressions:

$$\Phi_{p,d}(s) = \int \phi_p^{(d)}(s)ds,$$

$$\Psi_{p,d}(s) = \int s\phi_p^{(d)}(s)ds.$$

The finite weights used in the weak-form summation are constructed from differences of these antiderivatives evaluated at subdomain boundaries.

SUPPLEMENTARY NOTE 6: PIECEWISE LINEAR INTERPOLATION AND DECOUPLING OF INTEGRAL

This note provides the detailed derivation of the weight vectors $w_{\text{lhs},i}$ and $w_{\text{rhs},i}$ used in the discrete weak form. We begin by defining the interpolation basis, then show how the weak-form integrals decompose into weighted sums of nodal values.

To evaluate the weak form in practice, we work within the reference domain $s \in [-1, 1]$ of each subdomain and discretize it with M grid points s_i . Let $s_0 < s_1 < \cdots < s_{M-1}$ be partition points on the interval $[s_0, s_{M-1}]$, and suppose we are given values $x_i = x(s_i)$ and $f_i = f(x_i, s_i; \theta)$ for $i = 0, \dots, M-1$.

1. Linear Basis Functions. Define the piecewise linear Lagrange basis functions $\ell_i(s)$,

$$\ell_i(s) = \begin{cases} \frac{s - s_{i-1}}{s_i - s_{i-1}}, & s \in [s_{i-1}, s_i] \\ \frac{s_{i+1} - s}{s_{i+1} - s_i}, & s \in [s_i, s_{i+1}] & \text{for } 1 \le i \le M - 2. \\ 0, & \text{otherwise} \end{cases}$$

For the endpoints:

$$\ell_0(s) = \begin{cases} \frac{s_1 - s}{s_1 - s_0}, & s \in [s_0, s_1] \\ 0, & \text{otherwise} \end{cases} \qquad \ell_{M-1}(s) = \begin{cases} \frac{s - s_{M-2}}{s_{M-1} - s_{M-2}}, & s \in [s_{M-2}, s_{M-1}] \\ 0, & \text{otherwise} \end{cases}$$

2. Interpolant Construction. We define the linear interpolants of the functions x(s) and $f(u(s), s; \theta)$ as:

$$\tilde{x}(s) = \sum_{i=0}^{M-1} x_i \ell_i(s), \qquad \tilde{f}(s) = \sum_{i=0}^{M-1} f_i \ell_i(s).$$
 (S2)

These functions are continuous and piecewise linear. Note that if $x_i, f_i \in \mathbb{R}^D$ are vectors and $\ell_i(s) \in \mathbb{R}$ is a scalar, the terms $x_i\ell_i(s)$ and $f_i\ell_i(s)$ represent the standard scalar-vector products.

3. Projection Against a Test Function. We approximate the following integrals using Eq. (S2) as follows,

$$\frac{L}{2} \int_{s_0}^{s_{M-1}} f(x(s), s; \theta) \phi(s) ds \approx \frac{L}{2} \int_{s_0}^{s_{M-1}} \tilde{f}(s) \phi(s) ds = \sum_{i=0}^{M-1} f_i \left(\frac{L}{2} \int_{s_0}^{s_{M-1}} \ell_i(s) \phi(s) ds \right) = \sum_{i=0}^{M-1} f_i w_{\text{rhs}, i},$$

where the weights are defined as:

$$w_{\text{rhs},i} = \frac{L}{2} \int_{s_0}^{s_{M-1}} \ell_i(s) \phi(s) ds.$$

Similarly,

$$\int_{s_0}^{s_{M-1}} x(s)\phi'(s)ds \approx \int_{s_0}^{s_{M-1}} \tilde{x}(s)\phi'(s)ds = \sum_{i=0}^{M-1} x_i \left(\int_{s_0}^{s_{M-1}} \ell_i(s)\phi'(s)ds \right) = \sum_{i=0}^{M-1} x_i w_{\text{lhs},i},$$

where

$$w_{\mathrm{lhs},i} := \int_{s_0}^{s_{M-1}} \ell_i(s)\phi'(s)ds.$$

These weights can be precomputed for a fixed $\phi(s)$, independent of x.

4. Explicit Expression for Weights. For interior indices $1 \le i \le M-2$, we have:

$$\begin{split} w_{\mathrm{rhs},i} &= \frac{L}{2} \int_{s_{i-1}}^{s_i} \frac{s - s_{i-1}}{s_i - s_{i-1}} \phi(s) ds + \frac{L}{2} \int_{s_i}^{s_{i+1}} \frac{s_{i+1} - s}{s_{i+1} - s_i} \phi(s) ds \\ &= \frac{L}{2(s_i - s_{i-1})} \left[\Psi(s_i) - \Psi(s_{i-1}) - s_{i-1} (\Phi(s_i) - \Phi(s_{i-1})) \right] \\ &+ \frac{L}{2(s_{i+1} - s_i)} \left[s_{i+1} (\Phi(s_{i+1}) - \Phi(s_i)) - \Psi(s_{i+1}) + \Psi(s_i) \right], \end{split}$$

where $\Phi_{p,d}(s) = \int \phi_p^{(d)}(s) ds$ and $\Psi_{p,d}(s) = \int s \phi_p^{(d)}(s) ds$.

For the endpoints:

$$w_{\mathrm{rhs},0} = \frac{L}{2} \int_{s_0}^{s_1} \frac{s_1 - s}{s_1 - s_0} \phi(s) ds = \frac{L}{2(s_1 - s_0)} \left[s_1(\Phi(s_1) - \Phi(s_0)) - \Psi(s_1) + \Psi(s_0) \right],$$

and.

$$\begin{split} w_{\mathrm{rhs},M-1} &= \frac{L}{2} \int_{s_{M-2}}^{s_{M-1}} \frac{s - s_{M-2}}{s_{M-1} - s_{M-2}} \phi(s) ds \\ &= \frac{L}{2(s_{M-1} - s_{M-2})} \left[\Psi(s_{M-1}) - \Psi(s_{M-2}) - s_{M-2} (\Phi(s_{M-1}) - \Phi(s_{M-2})) \right]. \end{split}$$

The other weights can also be computed as follows:

$$\begin{split} w_{\text{lhs},i} &= \int_{s_{i-1}}^{s_i} \frac{s - s_{i-1}}{s_i - s_{i-1}} \phi'(s) ds + \int_{s_i}^{s_{i+1}} \frac{s_{i+1} - s}{s_{i+1} - s_i} \phi'(s) ds \\ &= \left[\frac{s - s_{i-1}}{s_i - s_{i-1}} \phi(s) \right]_{s_{i-1}}^{s_i} - \frac{1}{s_i - s_{i-1}} \int_{s_{i-1}}^{s_i} \phi(s) ds + \left[\frac{s_{i+1} - s}{s_{i+1} - s_i} \phi(s) \right]_{s_i}^{s_{i+1}} + \frac{1}{s_{i+1} - s_i} \int_{s_i}^{s_{i+1}} \phi(s) ds \\ &= -\frac{s_{i-1}}{s_i - s_{i-1}} \left[\Phi(s_i) - \Phi(s_{i-1}) \right] + \frac{1}{s_i - s_{i-1}} \left[\Psi(s_i) - \Psi(s_{i-1}) \right] \\ &+ \frac{s_{i+1}}{s_{i+1} - s_i} \left[\Phi(s_{i+1}) - \Phi(s_i) \right] - \frac{1}{s_{i+1} - s_i} \left[\Psi(s_{i+1}) - \Psi(s_i) \right]. \end{split}$$

For the endpoints, we similarly have:

$$w'_{\text{lhs},0} = \frac{s_1}{s_1 - s_0} \left[\Phi(s_1) - \Phi(s_0) \right] - \frac{1}{s_1 - s_0} \left[\Psi(s_1) - \Psi(s_0) \right],$$

$$w'_{\text{lhs},M-1} = -\frac{s_{M-2}}{s_{M-1} - s_{M-2}} \left[\Phi(s_{M-1}) - \Phi(s_{M-2}) \right] + \frac{1}{s_{M-1} - s_{M-2}} \left[\Psi(s_{M-1}) - \Psi(s_{M-2}) \right].$$

SUPPLEMENTARY NOTE 7: IMPLEMENTATION AND TRAINING DETAILS

Dataset Configuration After noise injection, the full time-series data is segmented into training samples using a sliding-window approach. Each sample consists of a trajectory segment of fixed length T, and in the strong formulation setting, the initial condition $y_0 \in \mathbb{R}^D$ is also included. Given a trajectory of length N, this yields N-T training examples of the form $\{y_0^{(i)}, \mathbf{y}^{(i)}\}_{i=1}^{N-T}$, where $y_0^{(i)} = x_i$ and $\mathbf{y}^{(i)} = \{x_i, x_{i+1}, \dots, x_{i+T-1}\}$. Trajectories are extracted with uniform stride to maintain temporal coherence, enabling efficient mini-batch training across strong, weak, and WP-NODE formulations.

Hyperparameters and Training Setup To support the different training objectives in the framework, the above dataset construction strategies are adopted depending on the loss formulation.

The key hyperparameter settings employed in the experiments are summarized below. Strong-form training uses fixed sequence lengths of 25 across all systems, while the WP-NODE uses shorter rollouts between 1 and 5 steps to reduce gradient instability. Details on the number of rollouts used for each case presented in the main article can be referred to Supplementary Table 1. For training components involving a weak-form loss (i.e., the weak NODE and WP-NODE modes), data is organized into integration subdomains. The subdomain size M is set to 60 for L63, 80 for L96, and 60 for the KS system. The number of overlapping subdomains K is chosen to be roughly half the total data length N, and the test function parameter p is set to 16, as these values were found empirically to yield optimal performance. The model is trained on the full time-series, since the weak-form loss targets integrated residuals over subdomains rather than pointwise supervision, making conventional overfitting to trajectory data less directly applicable.

Network Architecture and Optimization. All neural networks use the GELU activation function due to its consistent performance across tasks. Shallow architectures with 1–2 hidden layers are adopted to balance capacity and training stability. Training is performed using the Adam optimizer with minibatches. A batch size of 1024 (2048 for KS) is used across different ensemble runs. A carefully tuned learning rate scheduler and early stopping based on validation loss are used to ensure efficient training. A relatively large initial learning rate of 0.02 accelerates early convergence and is automatically decayed to refine performance.

For weak NODE and WP-NODE losses, models are trained for up to 20,000 epochs. In contrast, strong-form models are trained for fewer epochs (150–300, based on system complexity), due to higher computational cost and faster convergence. During inference, double-precision arithmetic is employed alongside the dopri5 solver to compute

	Number of rollouts \downarrow									
System	0%	1%	5%	10%	20%					
L63	1	2	2	1	2					
L96	1	1	2	2	1					
KS	1	1	1	1	5					

Supplementary Table 1. Number of rollouts used during WP-NODE training for each case in Table 1 of the main article.

all reference trajectories with double precision, ensuring sufficient accuracy for reliable evaluation.